

博士論文

Mitigating Porpoising in Planing Simulation of Seaplanes

（水上飛行機の滑走シミュレーションにおける

ポーポイズングの抑制）

Keiichi Ito

伊藤 景一

Abstract

The towing tank experiments conducted at the Yokohama National University from November 30 to December 9 in 2005, suggested a new way of suppressing a dangerous coupled motion between heave and pitch called porpoising. This research develops on the observations made in the experiments and conducts numerical simulations to further investigate the parametric design space. Two Linear-Time-Invariant models were developed: rigid-body planing craft (conventional float planes or flying boats) and flexibly supported planing craft. The latter can simulate the new method found in the experiments for suppressing porpoising. In this study, the stability of the oscillatory motions was analyzed to see the effect of design variables to the inception of porpoising. The parametric study of flexibly supported float planes in the context of porpoising is a new contribution to the conceptual design of seaplanes.

Dedication and Acknowledgements

The undergoing project of developing innovative seaplanes (project headed by Tatsumi Sakurai and the members of Hiyoh Aircraft Manufacturing and Development Co. and Aeromarine Systems Cooperation Association) is an endeavour supported by many dedicated and enthusiastic volunteers. The author would also like to expresses sincere gratitude to the reviewing committee for their critical and constructive feedback.

Nomenclature

β	Deadrise angle in [radians]
β_{deg}	Deadrise angle in [degrees]
ϵ	Thrust line angle with respect to the keel line (positive upwards) in [radians]
η_3, η_5	Displacement in heave and pitch respectively from the inertial coordinate x_b, z_b
\hat{y}	Estimated objective value from a weight vector in a Self-Organizing Map
λ_0	λ_w at the static equilibrium position
λ_w	Mean wetted length to beam ratio, $0.5(L_K + L_C)/B$
\mathbf{t}	Training sample point used in Self-Organizing Map
\mathbf{w}	Weight vector of a cell of a Self-Organizing Map
Ω	Multidimensional design space (a product space with upper and lower bounds in each dimension) with real design variables
\Re	Real variable set
$\Re(\sigma)_{\max}$	Maximum real part of the eigenvalues of a matrix \mathbf{K} as in $\dot{\mathbf{x}} = \mathbf{K}\mathbf{x}$, unit in [1/s]
ρ	Water density in $[kg/m^3]$
τ	Trim angle of planing area in [radians]

τ_{deg}	Trim angle of planing area in [degrees]
ξ_3, ξ_5	Displacement in heave and pitch respectively from the inertial coordinate x_a, z_a
a	Distance between CG and R_v (positive when pitch-down moment results) in [m]
a_{33}	Two-dimensional added mass of a wedge plunging into water in [kg/m]
A_{ij}	Hydrodynamic added mass/moment of inertia in the direction of i due to the motion in the direction of j
AHR	Average hull roughness in [μm]
B	Beam length (i.e. width) of a float in [m]
B_{ij}	Hydrodynamic damping coefficient in the direction of i due to the motion in the direction of j
C	Covariance matrix of selected weight vectors \mathbf{w}
c	Pitching moment arm of hydrodynamic resultant pressure force N with respect to CG (positive when pitch-down moment results), $l_{cg} - l_p$
C_F	Friction coefficient
$c_{f,b}$	Damping coefficients in the flexible support (front and back) in [$N s/m$]
C_{ij}	Hydrodynamic restoring force/moment coefficient in the direction of i due to the motion in the direction of j
C_{L_0}	Lift coefficient for zero deadrise angle ($\beta = 0$ [rad.])
C_{L_β}	Lift coefficient
d	Draft in [m]
f	Thrust line distance from CG (positive when pitch-up moment results) in [m]

F_{L_0}	Lift force for zero deadrise angle ($\beta = 0$ [rad.])
F_{L_β}	Lift force
F_{n_B}	Froude number based on the beam length defined as U/\sqrt{gB} , where g is gravitational acceleration
G	Set of finite number of samples from feasible region X
h	Neighborhood function used in training a Self-Organizing Map
I_A	Pitching mass moment of inertia of the aircraft without the floats for the flexible-support model in $[kg\ m^2]$
I_B	Pitching mass moment of inertia of the floats for the flexible-support model in $[kg\ m^2]$
I_{55}	Pitching mass moment of inertia of rigidly supported seaplane/model in $[kg\ m^2]$
$J(x)$	Objective function
K	$\frac{1}{\tan\beta} \left[\frac{\pi}{\sin\beta} \frac{\Gamma(1.5-\frac{\beta}{\pi})}{\Gamma^2(1-\frac{\beta}{\pi})\Gamma(0.5+\frac{\beta}{\pi})} - 1 \right]$, where Γ is the Gamma function
$k_{f,b}$	Spring constants in the flexible support (front and back) in $[N/m]$
L	Upper bound of a permissible objective value
L_C	Wetted chine length measured from the step in $[m]$
L_K	Wetted keel length measured from the step in $[m]$
l_p	Distance measured along the keel from the step to the center of hydrodynamic pressure in $[m]$
$l_{Af,Ab}$	Attachment locations of flexible supports on the aircraft relative to center of gravity of the aircraft in $[m]$
$l_{Bf,Bb}$	Attachment locations of flexible supports on the floats relative to center of gravity of the floats in $[m]$

l_{cg}	Longitudinal distance of center of gravity along the keel line measured from the step or transom in $[m]$
M	Mass of the aircraft for the rigid body model in $[kg]$
m_A	Mass of the aircraft for the flexible-support model in $[kg]$
m_B	Mass of the float for the flexible-support model in $[kg]$
M_t	Number of sample points for training Self-Organizing Maps
N	Resultant hydrodynamic pressure force acting on the planing surface in $[N]$
n	Number of design variables
N_f	Number simulation function calls
N_s	Number of simulation function calls that satisfied the stability criteria
R_n	Reynolds number UL_K/ν , where ν is the kinematic viscosity of water
R_v	Frictional force acting on the planing hull assumed to act parallel to keel line in $[N]$
T	Thrust force in $[N]$
t	Time in $[s]$
T_s	Selectivity parameter in SOMBAS that controls the probability of weight vectors from the Self-Organizing Map gets selected for mutation and evaluation
U	Planing speed in $[m/s]$
U_{lim}	Planing speed at which the planing craft becomes unstable in $[m/s]$
V	Vertical velocity with which the hull impacts the water surface, $U \tan \tau$
vcg	Vertical distance of CG from the keel line in $[m]$

X	“Feasible region” set whose element satisfy objective value condition $J(\mathbf{x}) < L$
x_a, z_a	Inertial coordinate moving with the aircraft’s CG’s equilibrium position without floats, x_a pointing horizontally to the stern, z_a pointing vertically upward
x_b, z_b	Inertial coordinate moving with the aircraft’s CG’s equilibrium position when the supports are rigid and moving along the floats’ CG’s equilibrium position when the supports are flexible, x_b pointing horizontally to the stern, z_b pointing vertically upward
x_T	x coordinate of transom stern or step, set equal to l_{cg}
y_{\min}	The smallest objective value among the training samples $\mathbf{t}(m)$
z_{\max}	Height above the undisturbed water surface where the maximum pressure on the V-shaped hull happens due to its impact to the water

Contents

0	Summary in Japanese	13
0.1	要約	13
0.2	制約	15
0.3	貢献	15
1	Introduction	17
1.1	Porpoising	17
1.2	Literature	19
1.3	Overview	20
2	Methods	23
2.1	The Numerical Model	24
2.2	Stable Design Search	25
2.3	Equations of Motion	29
2.4	Self-Organizing Map Based Adaptive Sampling	30
3	Results	35
3.1	Towing Tank Experiments	36
3.2	Rigid-Support Case	36
3.2.1	Conclusion of Rigid-Support Case	43
3.3	Flexible-Support Case	43
3.3.1	Conclusion of Flexible-Support Case	44
3.4	Oscillation Analysis	47
3.4.1	Conclusion of Oscillation Analysis	52
3.5	Sensitivity Analysis	53
3.5.1	Conclusion of Sensitivity Analysis	59
3.6	Design Subspace Search for Stable Designs	60
3.6.1	Conclusion for Design Subspace Search for Stable Designs	62
3.7	Parameter Setup for SOMBAS	65
4	Conclusion	69
4.1	Limitations	70
4.2	Contributions	71
4.3	Potential Developments	72
4.4	Closing Remarks	73

Chapter -1

A	Ovreview of Hydrodynamic Calculations	75
A.1	Trim Determination	75
A.2	Stability Derivatives	77
B	Dimensional Analysis	81
B.1	Non-Dimensional Parameter Gropus	81
C	Root-Locus Plots and $\Re(\sigma)_{max}$ Plots of Various Support Configurations	85
D	SOMBAS	89

Chapter 0

Summary in Japanese

0.1. 要約

本博士論文では、水上飛行機の平水面滑走時における安定性について考察する [1, 2]。2005年12月に横浜国立大学の水槽実験において双フロート模型の牽引実験を行った際、二つの興味深い現象が観察された [3]。一つは滑走速度が上昇しある値に達すると、ピッチングとヒービングが連成したポーポイジングと言う運動が起こり、じゃじゃ馬が暴れる様な不安定な状態になるが、その運動の抑制に重心を後方にずらす事が有効であった事。もう一つは、フロートと機体の間の支持構造を車のサスペンションに相当するような柔構造に置き換えた所、ポーポイジングの発現が抑制された事であった。何れも波のない平水面を滑走する際に確認した現象である。この事象を理解するために、2自由度の剛体線形モデルと柔支持構造を含む4自由度の線形モデルを作成しその挙動の再現を試みた。その結果、二つの線形モデルは、実験結果を定性的に再現した。また定量的にも振動の発散条件（滑走速度と重心位置）において比較的良好な一致を見せた。

滑走線形モデルは飛行力学の線形モデルと同様に微小擾乱を仮定し、状態変数（ピッチとヒーブ）及びその速度と加速度を考慮した。またダンピングを含む外力及び付加質量はFaltinsen [4] に準拠した。これはポテンシャル理論や水槽実験を基にした半実験式で成り立っている。

以上を元に、どのような条件によって滑走が不安定になるかパラメトリックに調査した。剛支持モデルに関しては、滑走面及び慣性を定義する設計パラメータに値を入れて、全ての振動モードが減衰する時を安定とした。また柔支持モデルに関しては、上記の設計パラメータに加えて前後柔

支持機のパラメータ、即ちばね係数とダンパー係数の値を様々に変える事によって発散モードの有無を調べた。具体的には、振動解析と感度解析を行って、発散振動モードの滑走速度による変化や設計変数の安定性への影響を調べた。また、設計パラメータを同時に変化させて安定な滑走を実現する値を探索する際に、独自に開発したアルゴリズム、**Self-Organizing Map Based Adaptive Sampling (SOMBAS)**を用いた [5, 6, 7]。このアルゴリズムを用いれば、目的関数がある閾値を満たす（ここでは線形モデルの固有値の実数解の最大値がゼロ以下になるような）多様な解を効率的に求める事が出来る。解は多次元のベクトルであるが、本研究ではこれを所望の二変数の分散図に投射することによって、各々の設計変数が固有値に及ぼす影響や、変数間の相関関係を調べた。

新たな知見として、ポーポイジングの発散振動は柔支持構造によってその発現が抑えられ、より高速の滑走速度においてフロートと機体が、ピッチ角で、ほぼ逆位相となる、より高い周波数の共振振動が発生する事が計算によって示唆された。この共振によって不安定になる滑走速度は、ばね係数とダンピング係数等を調節することによって変える事が出来る。よって、柔支持モデルは剛支持モデルより高速な速度まで、安定に滑走し得る事が示された。これは水槽実験の結果とも整合している。また、水上飛行機の重心の縦方向（つまり前後方向）移動は、柔支持においては不安定化に（必ずしも）繋がらない事や、フロートのビーム長（フロート幅）が重要である事が計算で示された。

SOMBASを使った解析では、柔支持ではビーム長が、ある特定の設計変数の上下限值内では、短い方がより安定なデザインを生成している。これは、フロート周りのピッチングによる付加質量の低減が上記の共振周波数を上げ、ポーポイジングの周波数との間隔を広げる事に貢献しているためと思われる。剛支持では逆にビーム長が長い方が水力学的なダンピングが効くため、安定なデザインを得られると推測される。ただし柔支持における共振は、現状の線形モデルでも多くの変数が連成し複雑であるため、正確な理解には更なる研究が必要である。

0.2. 制約

1. 水上飛行機の滑走安定性をテーマとしたが、水槽実験模型においても数値モデルにおいても尾翼や主翼の空力は考慮されていない。これは今後の研究の重要課題である。
2. 本研究では水槽実験の後に数値モデルを構築している。モデルの精度を上げるために、数値モデルによる予見を元に更なる水槽実験を行うのが望ましい。
3. フロートの水力学モデルは滑走面付近に限られ、水による動圧のみを考慮している。艇体先端部の湾曲面とステップ以後の艇体後部は考慮されていない。しかし既存の半実験式ではこれらの部位のモデル化は微小擾乱の範疇を超える。フロート全体を考慮したシミュレーションには、数値流体等の計算やそのための新たな実験が必要である。
4. 柔支持構造の制御について本論文では検討していないが、自動車同様、セミアクティブやアクティブサスペンション等、様々な可能性がある。

0.3. 貢献

1. ポーボイジングは水上飛行機の危険要因として古くから知られていたが、その発現条件はあまり良く分かっていなかった。これに対して、航空機設計においては、経験則に頼る所が多く、広範なパラメトリック調査は、私が知る限り皆無である。本研究は、水上飛行機概念設計において、水上滑走時の縦安定性をより詳細に考慮するための基盤を与えるものである。
2. 従来、ポーボイジング発現時に、重心を前後どちらに移動させればよいかは、一貫した知見が無かった。本研究は、その理由を縦方向に存在する不安定帯域の存在によるものであると示唆した。重心の位置が不安定帯域の前方にあれば、更に前方に重心を移動した方が

良く、逆に不安定帯域の後方にあれば、重心を更に後方にずらす方がよい。また、この不安定帯は速度が上がるほど、前後に拡張して行くと言う計算結果を得た。

3. 柔支持構造がポーポイズニングにもたらす影響を初めて数値モデルを用いて調査した。
4. 多次元変数空間をSOMBASと言うアルゴリズムを適用して得られた解集合より多数の設計変数が安定性に及ぼす影響を総合的に分析した。また数値モデルを用いた感度解析により、それらの設計変数が安定な滑走速度の限界値、或いは振動固有値に与える影響を解析した。またこれらによって新たな設計指針を得られる事を示した。

Chapter 1

Introduction

S EAPLANES and their amphibian versions have been largely a neglected type of aircraft in recent aviation except for very specific missions and in limited geographic regions. This is due to higher maintenance costs, less payload, and lower operational reliability (high waves are an additional weather hazard) compared to land based aircraft. However, recent technological advances in materials and computational capabilities along with macroeconomic and ecological considerations may render this type of aircraft interesting. Point-to-point operation in a coastal area could alleviate traffic congestion in urban airports and make remote islands more accessible. This, in turn, should help more balanced economic growth and better emergency services in smaller cities and rural areas. In this thesis, a century old problem particular to seaplanes called “porpoising” is addressed from a modern computational perspective. Progress in mitigating porpoising leads to safer design of seaplanes in waterborne planing condition.

1.1. Porpoising

Porpoising is a coupled oscillatory motion between heaving and pitching that can manifest when seaplanes are traveling on water at planing speed (Figure 1.1). This motion may become unstable and can pose significant risk to the safe operation of waterborne aircraft. Traditionally, the rules of thumb in designing of hulls and physical experiments [8, 9, 10, 11] (combined with pilot training [12, 13]) have been the methods of mitigating the risk. However, the phenomenon is poorly understood and sufficient parametric studies applicable to seaplanes have not appeared in the literature. Current research aims to fill this gap. The objective is to effectively

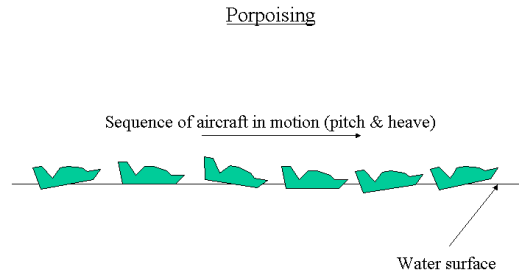


Figure 1.1: Schematic of porpoising

mitigate or eliminate porpoising by design.

Towing tank experiments [3] showed that the moving center of gravity aft, or employing flexible supports (between the aircraft and the floats) comparable to those of a car could improve the stability of the planing craft (Figure 1.2). To understand these observations, Linear-Time-Invariant models were constructed and the stability of oscillatory motions was studied. The numerical models were coherent with the experiments and two major design questions were answered, namely 1) the appropriate direction to move the center of gravity when porpoising is a problem [14], 2) whether flexible supports suppress porpoising globally or under certain conditions [3]. Parametric investigation of porpoising behavior based on numerical



Figure 1.2: An implementation of the Flexible Support System in an Ultra Light Plane

simulations and investigation of flexible supports for mitigation of porpoising are

two contributions of this thesis.

1.2. Literature

In the aeronautical engineering literature, there has been a series of efforts to theoretically describe longitudinal dynamics of planing seaplanes to explain porpoising through full-scale and towing tank experiments. An extensive review of this line of research is given in [15]. Perring and Glauert [16] introduced a theoretical approach to stability of the planing aircraft analogous to the stability of aircraft flight. They derived algebraic expressions for the stability derivatives with empirical coefficients. The report analyzed one and two-step planing characteristics including aerodynamic forces. It showed that radius of gyration i.e., the ratio between the moment of inertia and mass was important in representing the motion correctly and established that the surge component of the motion could be neglected. Later, Klemin, Pierson, and Storer [14] used extensive tank tests data [17] to replace the stability derivatives derived in [16]. Benson, Lindsay and Freihofner [18, 19] presented methods and charts for computing stability derivatives of a longitudinally straight v-bottom planing surface representing the forebody of a seaplane. They used extensive towing tank test data reported by Shoemaker [20] to plot the charts. However, these early developments depended on “experimental constants that are not more easily determined than a direct experimental determination of stability” [21].

More recently, porpoising has also been investigated in the naval engineering context, such as in the work by Celano [22] and Ikeda [23], by conducting tank tests of a few different prismatic (i.e. v-bottom) hull models. The seminal work by Savitsky [24] compiled the elemental hydrodynamic characteristics of prismatic planing surfaces by deriving empirical planing equations. The equations are the lift, drag, wetted area, center of pressure, and porpoising stability limits of planing surfaces as a function of speed, trim angle, deadrise angle, and loading. The work opened up the possibility of computational procedures to do conceptual designs of planing hulls. Fundamental research investigating “slamming” by naval architects also led to the understanding of planing surfaces. In particular, wedge-

drop tests [25, 26] and potential theory modeling [27, 28] led to the estimation of pressure distribution on the prismatic hull and the added mass of the water on the hull. In 2006, Faltinsen published a book dedicated entirely to hydrodynamics of high-speed marine vehicles in which a unified and detailed exposition of porpoising could be found [4].

This thesis builds on these contributions to enable simple computational models to perform more extensive parametric investigation (current work demonstrates investigation of 7 parameters simultaneously as opposed to 2 to 3 parameters in literature) enabling analysis of new ideas to mitigate porpoising.

1.3. Overview

This work addresses one of the drawbacks of seaplanes called porpoising which is a dynamic instability in planing seaplanes and high-speed boats [29]. The objective of the thesis is to advance the technology for mitigating the phenomenon from the conceptual design stage. In this chapter, we have introduced porpoising and a new finding (a flexible support system between the aircraft and float) that may be effective in mitigating this century-old problem. The literature survey has also been given to outline the past effort in analyzing the longitudinal stability of a planing craft. In Chapter 2, we describe the numerical models and an algorithm that was used in analyzing the stability of a planing craft and finding stable designs called SOMBAS. Here, a new solution search method is described that performs a feasible region identification. Given a simulation model (or a function) the algorithm searches for a set of solution that satisfy certain threshold in the objective value. Furthermore, the algorithm increases the diversity of such solutions and eventually returns a set of diverse solutions that satisfy the objective value threshold filling a “feasible region” in the input variable space. In Chapter 3, we present the results obtained from the numerical experiments and check its validity in view of the experimental results. Chapter 4 discusses the implications of the results as well as potential future directions and concludes the thesis. Further details on the hydrodynamic calculations are given in Appendix A. Non-dimensional parameters are

derived in Appendix B and an abridged information of the tow-tank experiment conducted at Yokohama National University is given in Appendix 3.1. Finally, the pseudo codes of the algorithm (SOMBAS) used in the search of stable designs are given in Appendix D.

The core part of this thesis has been presented at AIAA Aviation conference in 2015 [1] and published in Journal of Aircraft in 2016 [2]. SOMBAS [5, 6] was developed as a part of a research program sponsored by the Flemish government which led to a doctoral degree in 2016 [7].

Chapter 2

Methods

THE first step in this study was to numerically recreate at least qualitatively the observation made in the towing tank experiments. Particularly, the objective here is to confirm that the inception of porpoising occurs at approximately 5 m/s of towing speed with the original CG location, and that by moving the CG aft stabilizes the towed model. Then, observe numerically that the flexible support “stabilizes” the towed model. The second step was to explore different designs by varying parameters in the numerical model. The towed model consisted of a pair of floats in catamaran configuration and a frame on top of it (Figure 2.1). The frame has adjustable weights to roughly simulate the inertia characteristics of the aircraft that the float was designed for, which is a 1/3 scale Piper Cub. By changing the location of weights, one can also move the location of the CG backward or forward. In the following, the numerical model of the conventional rigid case and then the flexibly supported case are described.



Figure 2.1: Experiment with the flexible support at the towing tank of Yokohama National University

2.1. The Numerical Model

For the numerical analysis, the catamaran configuration was replaced by a mono-hull representation of prismatic hull as shown in Figure 2.2. The transom location in this figure corresponds to the step location in the actual float. The afterbody of the float is neglected in the modelling and so is the curved front portion of the forebody of the float. The dynamic stability was computed using small perturbation analysis as presented in Faltinsen [4]. The coordinate systems employed are shown in Figure 2.4. For the rigidly supported case, the inertial coordinate system x_b, z_b was set to move along with the towed craft, its origin coincides with the equilibrium position of the craft's center of gravity. The x axes point to the stern of the craft. For the flexibly supported case, separate inertial coordinate systems that move along the craft were employed for above the support x_a, z_a and the float x_b, z_b . These are an approximate way to represent the dynamics (for the frame has surge component of motion that are neglected) but were done in order to facilitate the analysis. The linear system of equation for the rigidly supported case is equation (2.1), and for the flexibly supported case, equation (2.2). Added mass A_{ij} , damping force coefficient B_{ij} , and the restoring force coefficient C_{ij} were formulated according to chapter 8 and 9 of Faltinsen's book [4]. A cursory description of how A_{ij} , B_{ij} , and C_{ij} are computed is given in the appendix. The numbers in subscripts $i, j \in \{3, 5\}$ denote heaving ₃ and pitching ₅ respectively. The first subscript i refers to the resulting force or moment direction and the second subscript j refers to the motion causing the force or moment. For example, C_{35} refers to the heaving force coefficient due to pitching motion. One can also find relevant information on the hydrodynamic forces for planing crafts in [30, 23, 14, 19].

The flexibly supported case contains additional parameters on the characteristics of the support, namely the spring constants k_f, k_b and the damping coefficients c_f, c_b . The subscripts denote their locations: f for front and b for back. Likewise, the attachment locations relative to center of gravity are denoted l_{Af}, l_{Ab} for the front and back attachment point on the aircraft side respectively, and l_{Bf}, l_{Bb} on the float side. These parameters are visualized in Figure 2.3. We have kept the

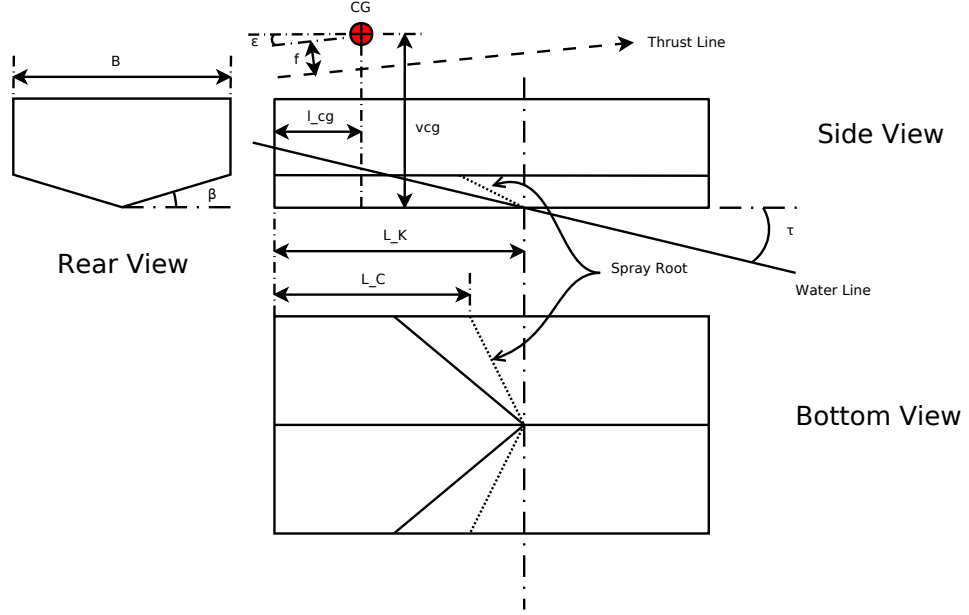


Figure 2.2: Diagram of planing hull cut-out.

attachment points fixed and varied the spring constants and damping coefficients in our numerical simulations. The equation of motion of both the rigid and flexible case are described in section 2.3.

Note that, although the linear-time-invariant (LTI) models are “linear” with respect to state variables, they are non-linear systems with respect to design variables when it comes to computing eigenvalues and stability limits of their planing speeds. The LTI models are computed with respect to the trim position for a given planing speed. The trim position(trim angle and draft) is also a non-linear function of the design variables, the weights, and the planing speed.

2.2. Stable Design Search

In the rigidly supported case, we also used Self-Organizing Map Based Adaptive Sampling (SOMBAS) [6, 7] to search for stable designs. SOMBAS is suitable for the task of searching for multiple and diverse solutions satisfying certain objective conditions. A complete description of SOMBAS’ algorithm is given in section 2.4. We searched for designs with negative values in maximum real part of the eigenvalues. For the two-design-variable case, we use the longitudinal distance of CG along

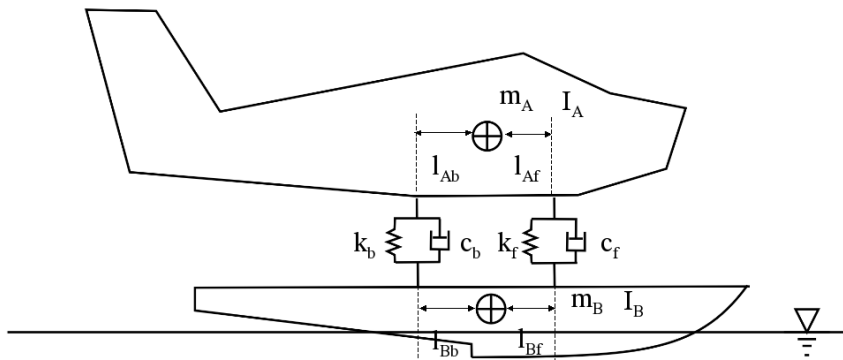


Figure 2.3: Schematic of a float plane with the flexible support

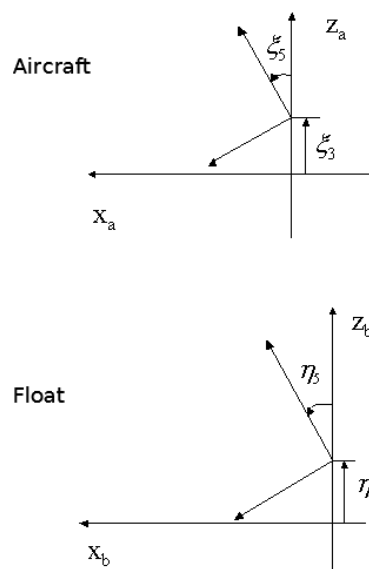


Figure 2.4: Coordinate system for the Small Perturbation Method

the keel line l_{cg} measured from the step or transom, and vertical distance of CG from the keel line vcg . For the seven-design-variable case, we use the beam length B , the deadrise angle β_{deg} , the pitching moment of inertia I_{55} , the thrust line distance f from CG (positive when pitch-up moment results) and the thrust line angle with respect to the keel line (positive upwards) ϵ . Figure 2.2 shows a diagram describing the design variables except the inertial variable I_{55} .

$$(2.1) \quad \begin{pmatrix} M + A_{33} & A_{35} & 0 & 0 \\ A_{53} & I_{55} + A_{55} & 0 & 0 \\ 0 & 0 & 1 & 0 \\ 0 & 0 & 0 & 1 \end{pmatrix} \begin{pmatrix} \tilde{\eta}_3 \\ \tilde{\eta}_5 \\ \tilde{\eta}_3 \\ \tilde{\eta}_5 \end{pmatrix} + \begin{pmatrix} B_{33} & B_{35} & C_{33} & C_{35} \\ B_{53} & B_{55} & C_{53} & C_{55} \\ -1 & 0 & 0 & 0 \\ 0 & -1 & 0 & 0 \end{pmatrix} \begin{pmatrix} \eta_3 \\ \eta_5 \\ \eta_3 \\ \eta_5 \end{pmatrix} = \begin{pmatrix} 0 \\ 0 \\ 0 \\ 0 \end{pmatrix}$$

$$(2.2) \quad \begin{pmatrix} c_f + c_b & c_f l_{Af} - c_b l_{Ab} & k_f + k_b & k_f l_{Af} - k_b l_{Ab} & -c_f l_{Bf} + c_b l_{Bb} & -c_f - c_b & c_f l_{Af} - k_b l_{Ab} & k_f l_{Af} - k_b l_{Ab} & c_f l_{Af} - c_b l_{Ab} & c_f l_{Af} - c_b l_{Ab} \\ c_f l_{Af} - c_b l_{Ab} & c_f l_{Af}^2 + c_b l_{Ab}^2 & k_f l_{Af} - k_b l_{Ab} & k_f l_{Af}^2 + k_b l_{Ab}^2 & -c_f l_{Af} l_{Bf} - c_b l_{Ab} l_{Bb} & -c_f l_{Af} + c_b l_{Ab} & k_f l_{Af} + k_b l_{Ab} & k_f l_{Af}^2 + k_b l_{Ab}^2 & c_f l_{Af}^2 + c_b l_{Ab}^2 & c_f l_{Af}^2 + c_b l_{Ab}^2 \\ -1 & 0 & 0 & 0 & 0 & 0 & 0 & 0 & 0 & 0 \\ 0 & -1 & 0 & 0 & 0 & 0 & 0 & 0 & -1 & 0 \\ -c_f - c_b & -c_f l_{Af} + c_b l_{Ab} & -k_f - k_b & -k_f l_{Af} + k_b l_{Ab} & B_{33} + c_f l_{Bf} + c_b l_{Bb} & B_{33} + c_f + c_b & -k_f l_{Af} + k_b l_{Ab} & -k_f l_{Af} + k_b l_{Ab} & -c_f l_{Af} + c_b l_{Ab} & -c_f l_{Af} + c_b l_{Ab} \\ -c_f l_{Bf} + c_b l_{Bb} & -c_f l_{Af} l_{Bf} - c_b l_{Ab} l_{Bb} & -k_f l_{Bf} + k_b l_{Bb} & -k_f l_{Af} l_{Bf} - k_b l_{Ab} l_{Bb} & B_{55} + c_f l_{Bf}^2 + c_b l_{Bb}^2 & B_{55} + c_f l_{Bf} - c_b l_{Bb} & C_{33} + k_f + k_b & C_{33} + k_f l_{Bf} - k_b l_{Bb} & C_{55} + c_f l_{Bf}^2 + c_b l_{Bb}^2 & C_{55} + c_f l_{Bf} - c_b l_{Bb} \\ 0 & 0 & 0 & 0 & 0 & -1 & 0 & 0 & 0 & 0 \\ 0 & 0 & 0 & 0 & 0 & 0 & 0 & 0 & -1 & 0 \end{pmatrix} \begin{pmatrix} \xi_3 \\ \xi_5 \\ \xi_3 \\ \xi_5 \\ \eta_3 \\ \eta_5 \\ \eta_3 \\ \eta_5 \\ \eta_3 \\ \eta_5 \end{pmatrix} = \begin{pmatrix} 0 \\ 0 \\ 0 \\ 0 \\ 0 \\ 0 \\ 0 \\ 0 \\ 0 \\ 0 \end{pmatrix}$$

2.3. Equations of Motion

The rigid-support case can be formulated as following.

$$(M + A_{33})\ddot{\eta}_3 + B_{33}\dot{\eta}_3 + C_{33}\eta_3 + A_{35}\dot{\eta}_5 + B_{35}\dot{\eta}_5 + C_{35}\eta_5 = 0 \quad (2.3)$$

$$(A_{55} + I_{55})\ddot{\eta}_5 + B_{55}\dot{\eta}_5 + C_{55}\eta_5 + A_{53}\dot{\eta}_3 + B_{53}\dot{\eta}_3 + C_{53}\eta_3 = 0 \quad (2.4)$$

where equation (2.3) describes the heave motion and equation (2.4) the pitch motion.

The flexible support case consists of equations of motion of two components: the aircraft and the float system (including the flexible support). Equation (2.5) describes the heaving motion of the aircraft and equation (2.6) describes the pitching of the aircraft. On the other hand, equation (2.7) describes the heaving motion of the float system and equation (2.8) its pitching motion.

$$\begin{aligned} m_A \ddot{\xi}_3 &= k_f(\eta_3 - \xi_3) + k_b(\eta_3 - \xi_3) \\ &+ k_f(l_{Bf}\eta_5 - l_{Af}\xi_5) + k_b(-l_{Bb}\eta_5 + l_{Ab}\xi_5) \\ &+ c_f(\dot{\eta}_3 - \dot{\xi}_3) + c_b(\dot{\eta}_3 - \dot{\xi}_3) \\ &+ c_f(l_{Bf}\dot{\eta}_5 - l_{Af}\dot{\xi}_5) + c_b(-l_{Bb}\dot{\eta}_5 + l_{Ab}\dot{\xi}_5) \end{aligned} \quad (2.5)$$

$$\begin{aligned} I_A \ddot{\xi}_5 &= l_{Af} [k_f(\eta_3 - \xi_3) + k_f(l_{Bf}\eta_5 - l_{Af}\xi_5)] \\ &- l_{Ab} [k_b(\eta_3 - \xi_3) + k_b(-l_{Bb}\eta_5 + l_{Ab}\xi_5)] \\ &+ l_{Af} [c_f(\dot{\eta}_3 - \dot{\xi}_3) + c_f(l_{Bf}\dot{\eta}_5 - l_{Af}\dot{\xi}_5)] \\ &- l_{Ab} [c_b(\dot{\eta}_3 - \dot{\xi}_3) + c_b(-l_{Bb}\dot{\eta}_5 + l_{Ab}\dot{\xi}_5)] \end{aligned} \quad (2.6)$$

$$\begin{aligned} (m_B + A_{33})\ddot{\eta}_3 &= -B_{33}\dot{\eta}_3 - C_{33}\eta_3 - A_{35}\dot{\eta}_5 - B_{35}\dot{\eta}_5 - C_{35}\eta_5 \\ &- k_f(\eta_3 - \xi_3) - k_b(\eta_3 - \xi_3) \\ &- k_f(l_{Bf}\eta_5 - l_{Af}\xi_5) - k_b(-l_{Bb}\eta_5 + l_{Ab}\xi_5) \\ &- c_f(\dot{\eta}_3 - \dot{\xi}_3) - c_b(\dot{\eta}_3 - \dot{\xi}_3) \\ &- c_f(l_{Bf}\dot{\eta}_5 - l_{Af}\dot{\xi}_5) - c_b(-l_{Bb}\dot{\eta}_5 + l_{Ab}\dot{\xi}_5) \end{aligned} \quad (2.7)$$

$$\begin{aligned} (I_B + A_{55})\ddot{\eta}_5 &= -A_{53}\dot{\eta}_3 - B_{53}\dot{\eta}_3 - C_{53}\eta_3 - B_{55}\dot{\eta}_5 - C_{55}\eta_5 \\ &- l_{Bf} [k_f(\eta_3 - \xi_3) + k_f(l_{Bf}\eta_5 - l_{Af}\xi_5)] \\ &+ l_{Bb} [k_b(\eta_3 - \xi_3) + k_b(-l_{Bb}\eta_5 + l_{Ab}\xi_5)] \end{aligned}$$

$$\begin{aligned}
 & - l_{Bf} [c_f(\dot{\eta}_3 - \dot{\xi}_3) + c_f(l_{Bf}\dot{\eta}_5 - l_{Af}\dot{\xi}_5)] \\
 & + l_{Bb} [c_b(\dot{\eta}_3 - \dot{\xi}_3) + c_b(-l_{Bb}\dot{\eta}_5 + l_{Ab}\dot{\xi}_5)]
 \end{aligned} \tag{2.8}$$

2.4. Self-Organizing Map Based Adaptive Sampling

In engineering design efforts, we often seek to optimize a set of design variables so that we minimize certain quantity of interest. However, this is not an easy task even with the availability of modern computer resources and numerical simulations (or simply models). For one thing, designs and models are developed progressively and are never completely accurate. For another, the more the models become accurate, the more computationally expensive they become. Furthermore, complex models often have large numbers of input variables that make the optimization of such system very difficult (“curse of dimensionality”). Self-Organizing Map Based Adaptive Sampling (SOMBAS) was conceived to alleviate such difficulties [7]. The explanation of the algorithm below closely follows that of previously published work [6, 7].

SOMBAS searches for a set of solutions that satisfy certain upper bound criteria for the quantity to be minimized. For our current purpose, SOMBAS can be used to obtain a set of hull designs that would not cause longitudinal instabilities. Specifically, SOMBAS tries to find a set

$$G \subseteq X = \{\mathbf{x} \in \Omega \mid J(\mathbf{x}) < L\},$$

where Ω is the multidimensional design space with the number of dimension n corresponding to the number of real design variables, $J : \mathbb{R}^n \rightarrow \mathbb{R}$ is an objective function, and L is an upper bound of a permissible objective value. Figure 2.5 shows the overall flow of the algorithm. The algorithms in pseudo codes can be found in Appendix D.

The first step of the algorithm is to collect a set of points (or experiments) from the design space Ω . This can be done with a random sampling method or with a design-of-experiment method. This set is used as the initial training set for the Self-Organizing Map (SOM). The training set is a matrix of M_t rows and $n + 1$ columns, where M_t is the number of training sample points specified by the user and n is the

2.4 Self-Organizing Map Based Adaptive Sampling

number of input design variables. The last column is the objective value we want to minimize below L , a parameter specified by the user.

Next, SOM is trained based on the sample set. SOM in this work is represented as a two-dimensional square grid of cells. Each of these cells has a weight vector associated with it. In this work, the weight vector \mathbf{w} is a set of continuous design variables that represents an instance of a possible new solution. We initially assign random numbers to the vector elements. Then, the weight vectors are learned from the set of training samples. The trained weight vectors can be considered to be a finite sample representation of the training sample distribution. The weight vectors \mathbf{w}_j are updated using the following equation for a given training sample \mathbf{t} .

$$\mathbf{w}_j(k+1) = \mathbf{w}_j(k) + h_{cj}(k) [\mathbf{t}(m) - \mathbf{w}_j(k)], \quad (2.9)$$

where j is a spatial index that identifies the cells in SOM, k is the training iteration index, $m \in \{1, 2, \dots, M_t\}$ is the training sample index running through each iteration of k , h_{cj} is a neighborhood function that depends on the distance between \mathbf{w}_c and \mathbf{w}_j on the map where \mathbf{w}_c is the closest weight vector to the training sample $\mathbf{t}(m)$ in the Euclidean sense. The neighborhood function decreases as the distance between the cells becomes far apart on the map. Thus, given a training sample and the closest matching weight vector, the farther cells on the map receive less influence of the weight update. The shape and magnitude of $h_{cj}(k)$ are changed as k increases in such a way that the second term (the weight update term) on the right-hand side of equation (2.9) reduces the radius and magnitude of influence.

A subset of the trained weight vectors are selected for further processing. The probability of a weight vector being selected depends on how close its objective value estimate is to the known smallest value. Note that the objective values in the weight vectors of SOM are estimates. The selection condition is

$$r < \exp\left(\frac{y_{\min} - \hat{y}}{T_s}\right), \quad (2.10)$$

where $0 \leq r < 1$ is a random number drawn from a uniform distribution, y_{\min} is the smallest output in the training sample, and \hat{y} is the estimated objective value from the weight vector. The temperature $0.01 \leq T_s \leq 10$ defines how selective the condi-

Chapter 2 Methods

tion is and a smaller value of T_s results in fewer new samples added to the training data set. The pseudo code of this selection condition is given in Algorithm 2.

We consider a case in which we seek to minimize an objective value y below certain threshold L . Below this threshold, diversity of solutions is sought. We call such a search as *feasible region identification* or *feasible region search*. One idea is to use a merit function similar to those described in [31]. One could give a better chance of being selected to points (i.e. cell weight vector) that are distant from existing training samples regardless of y value. To achieve this, we propose the following formula for the merit function.

$$F = \max(L, y) - \rho \min(\|\mathbf{x} - \mathbf{t}(m)\|_2), \quad m = 1, 2, \dots, M_t \quad (2.11)$$

where \mathbf{x} is the input vector for which F needs to be minimized, $\mathbf{t}(m)$ is a set of target samples from which minimum distance to the input vector \mathbf{s} is calculated, M_t is the number of such target vectors, and ρ is a weight constant. Unlike Torczon's merit function, our merit function incorporates a "truncation" value L below which only the separation from other target vectors $\mathbf{t}(m)$ matters. To minimize this merit function, one needs $y < L$ and maximize the distance to the nearest target vector $\min(\|\mathbf{s} - \mathbf{t}(m)\|_2)$. In our case, target vectors are the training set and the input vector \mathbf{s} is the selected weight vector from SOM. The algorithm to replace the output with this merit function is described in Algorithm 3. If \hat{y} is greater than the threshold L , both \hat{y} and the new weight vector's distance from the training set are taken into account. If \hat{y} is less than L , then the distance to the nearest training vector is the only term affecting the objective value and smaller F is obtained when the weight vector's distance to the nearest neighbor is larger. The ρ in equation 2.11 is a positive weighing constant

Mutation, as described in Algorithm 4, is applied to the selected weight vectors. We use the weight vectors as the centers of multivariate Gaussian distributions. The covariance matrix is obtained from the selected weight vectors. We use an idea similar to CMA-ES [32] to update the covariance matrices. The covariance matrix in the current iteration is combined with the covariance matrix computed in the previous iteration: $0.2C + 0.8C_{old}$. This is to avoid adapting too quickly to a local

2.4 Self-Organizing Map Based Adaptive Sampling

minimum. On top of that, we multiply a factor which is different whether the previous iteration produced a new minimum or not. If the previous iteration achieved a new minimum, we apply an expansion factor F_e , to which we assign a real value larger than 1. On the other hand, if the previous iteration did not produce a new minimum, we multiply a contraction factor F_c , to which we assign a real value between 0 and 1. The covariance matrix is the same for all the selected weight vectors. Each weight vector is perturbed by sampling from the multivariate Gaussian distribution. Mutation is very important to avoid premature convergence in SOMBAS.

After the perturbation of new samples, the training set is updated. Algorithm 5 and Algorithm 6 are two such methods. Algorithm 5 has a faster convergence but is more prone to lose diversity in the training set prematurely compared to Algorithm 6. In the latter method, if $\max(L, y)$ of the new perturbed sample and that of the randomly selected training sample are the same, the replacement of the selected training sample takes place only if the new perturbed sample has a larger distance to its nearest neighbor than the distance of the training sample to its nearest neighbor. Otherwise, the new perturbed sample replaces the training sample when the new sample has a smaller objective value. The nearest neighbors are searched among all the sampled points. We used Algorithm 6.

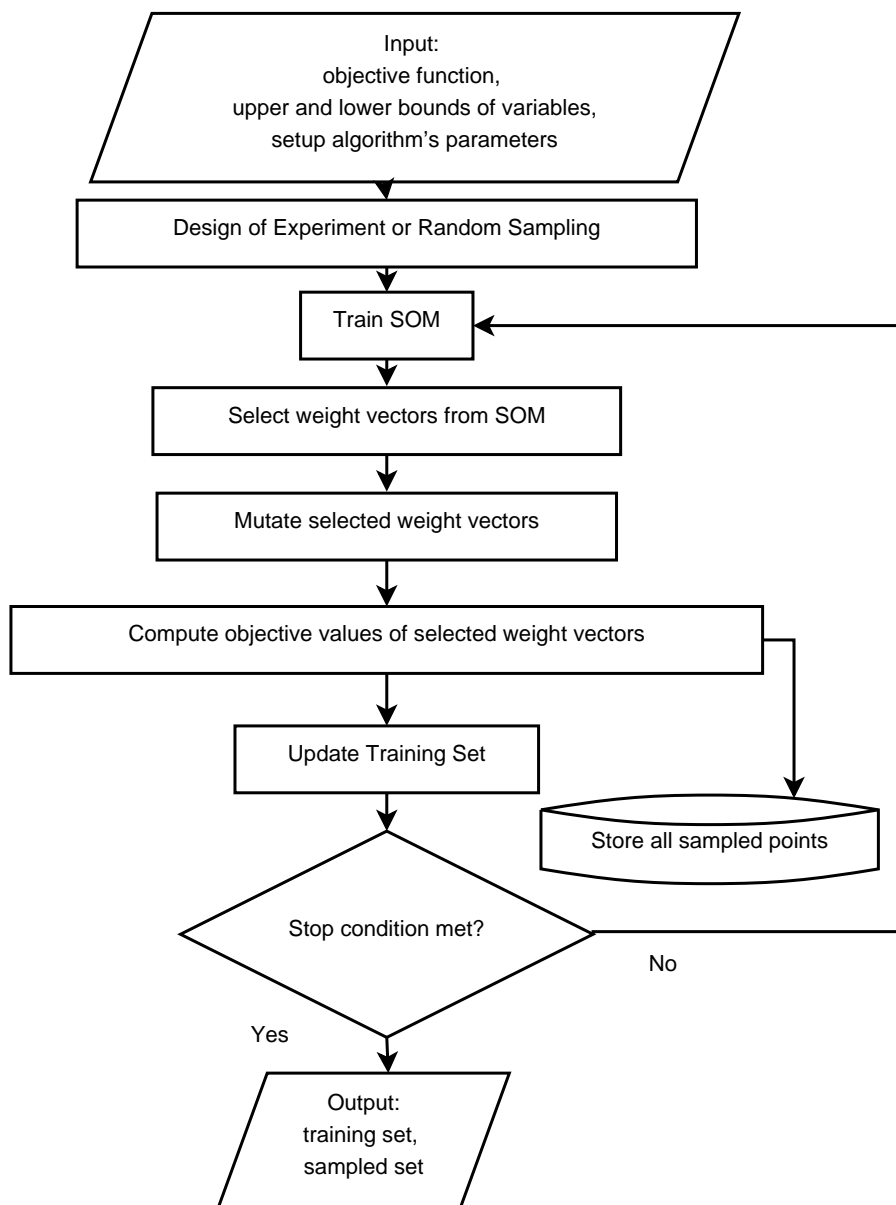


Figure 2.5: High level flowchart of SOMBAS.

Chapter 3

Results

FOR our purpose of discussing the results, we will first briefly review the tow-tank experiment. Figure 3.1 give the physical setup and schematic description of the towing system and the towed model and Figure 3.2 gives two sets of time series plot of sensor data obtained when towing speed was 7 [m/s]: one for the rigid support case and the other for the flexible support case. Pertinent description of the experiment [3] are summarized in section 3.1.

Figure 3.3 - Figure 3.5 and Figure 3.21 - Figure 3.22 are for the rigidly supported case and Figure 3.6 - Figure 3.9 are for the flexibly supported case. Nominal conditions for the calculation are as following unless otherwise specified: the planing speed $U = 6.0$ [m/s], the mass of craft for the rigid case $M = 16.18$ [kg] and for the flexible case $m_A = 10.79$ [kg] (aircraft), $m_B = 5.39$ [kg] (float), the beam length $B = 0.2$ [m], the moment of inertia for the rigid case $I_{55} = 5.981$ [kg m²], for the flexible case $I_A = 4.351$ [kg m²] (aircraft), $I_B = 1.630$ [kg m²] (float), the length along the keel from step to center of gravity $l_{cg} = 0.104$ [m] (assuming step location at 50 % of float length), the distance of CG from the keel $v_{cg} = 0.453$ [m], and the moment arm length from CG to the supports (Figure 2.3) are $l_{Af} = l_{Ab} = l_{Bf} = l_{Bb} = 0.2$ [m]. Froude number is defined based on the beam length $F_{nB} = U / \sqrt{gB}$. The beam length B and l_{cg} are not reported in Hirakawa's paper [3] and their values are educated guesses. In the simulation, we use the half body representation. That means we half the mass and moment of inertia in the calculations, and model as a mono-hull float plane. Dimensional analysis to obtain non-dimensional parameter groups is described in Appendix B.

3.1. Towing Tank Experiments

In the following, experimental results given in Hirakawa's paper [3] is briefly reiterated. The towing system were developed at the National University of Yokohama [3]. The tow-tank experiments were conducted from November 30 to December 9 in 2005.

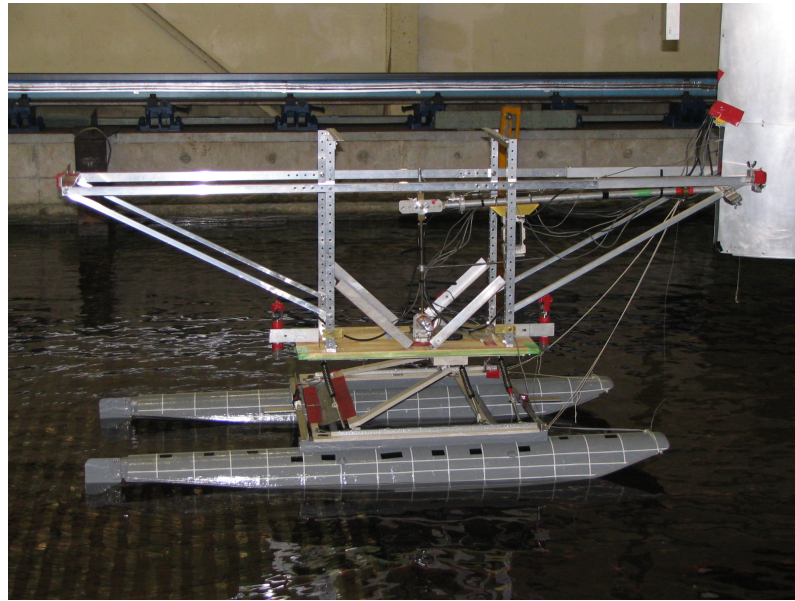
The upper structure of the towed model was dynamically similar to the 1/3 scale aircraft in terms of weight and moment of inertia. Aerodynamic similarities were not considered in the experiments. The rotational position of the guiding arms were measured using three potentiometers (Pot.1, Pot.2, and Pot.3). Heave and pitch motions are calculated based on these measurements. The relative position of the dummy aircraft with respect the float were measured using ultrasound distance sensors. Accelerations were measured using accelerometers. The side view of the setup of the towing system can be seen in Figure 3.1a and the arrangement of sensors are visualized schematically in Figure 3.1b.

Time histories of measurements and calculated heave and pitch motions are given in Figure 3.2. Figure 3.2a is a case when the supporting mechanism between the float and the dummy aircraft is rigid and Figure 3.2b is a case with the flexible support system. The towed speed for these two cases were 7 m/s and the rigid support case (Figure 3.2a) shows oscillation in heave and pitch indicating porpoising. At the standard CG location (Table 3.1), porpoising has been observed for towing speeds of 5 m/s and above for the rigid support case. Porpoising period was 0.84 seconds however the natural period of the towed model in pitch was 0.76 seconds. For the flexible support case, the oscillation did not manifest for all the towing speed tested (up to 7 m/s).

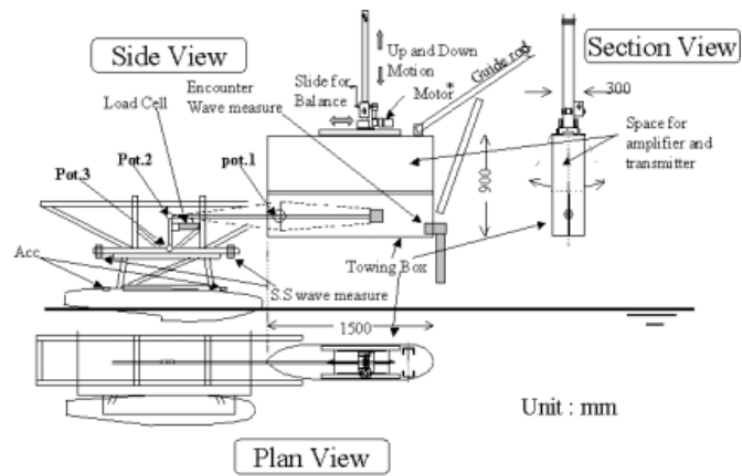
3.2. Rigid-Support Case

For plots with vertical axis showing the maximum eigenvalue $\Re(\sigma)_{\max}$ of the linear system, any positive value of the real part of the eigenvalue signifies divergence of the oscillation mode and therefore is unstable. The eigenvalues are calculated from the matrix obtained in the following way. $\mathbf{K} = \mathbf{M}^{-1}(-\mathbf{R})$, where $\mathbf{M}\dot{\mathbf{x}} + \mathbf{R}\mathbf{x} = 0$ and

3.2 Rigid-Support Case



(a) Physical set up



(b) Schematics of the measurement system [3]

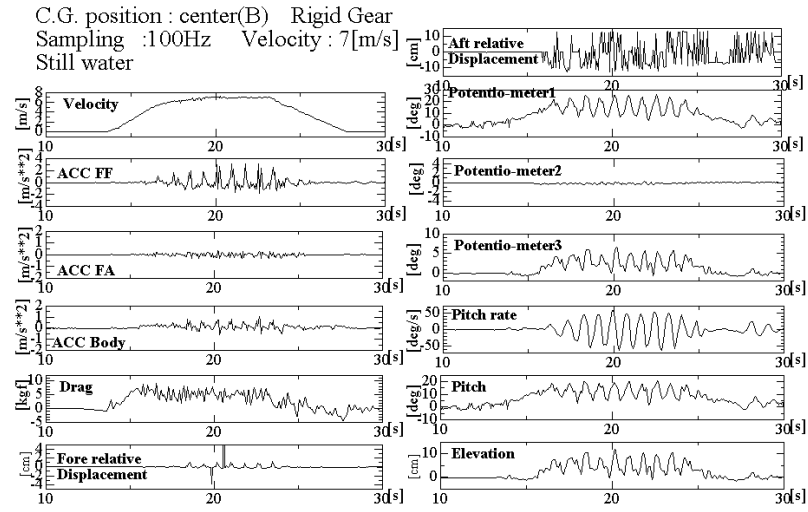
Figure 3.1: The towed model and the measurement system

Chapter 3 Results

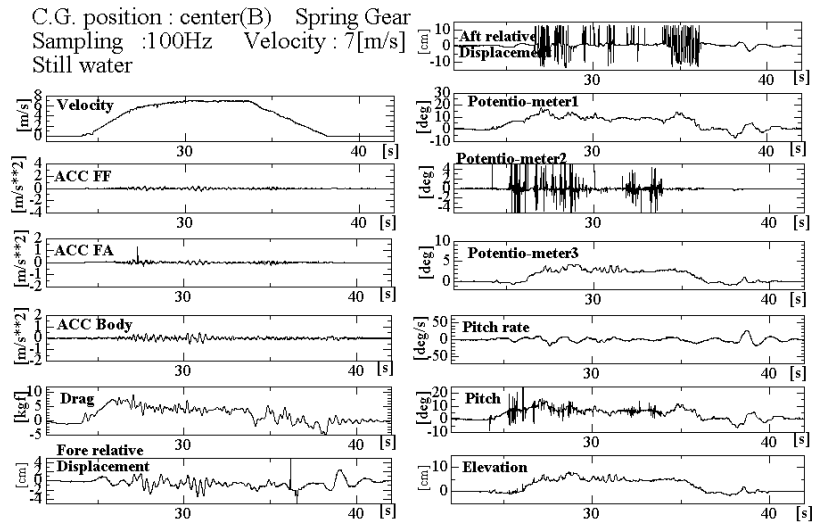
Float (including support)	Length	1.54 [m]
	Width	0.730 [m]
	Weight	5.39 [kg]
	CG height from keel	0.146 [m]
	CG location from the front tip of the float	0.743 [m]
	Pitch radius of gyration	0.550 [m]
	Roll radius of gyration	0.310 [m]
Structure	Yaw radius of gyration	0.486 [m]
	Weight (without the support)	9.15 [kg]
Combined	Total weight	16.18 [kg]
CG Standard	CG height from keel	0.453 [m]
	CG location from the front tip of the float	0.666 [m]
	Pitch radius of gyration	0.608 [m]
CG Backward	CG height from keel	0.453 [m]
	CG location from the front tip of the float	0.764 [m]
	Pitch radius of gyration	0.799 [m]

Table 3.1: Dimensions of the towed model

3.2 Rigid-Support Case



(a) Measurements from a rigidly supported case [3]



(b) Measurements from a flexibly supported case [3]

Figure 3.2: Sensor measurements from two experiments

Chapter 3 Results

x is the state vector, where \mathbf{M} and \mathbf{R} represent the matrices in equation (2.1) and equation (2.2).

Figure 3.3 confirms that moving the CG backwards towards the step helps the craft to remain stable until a higher velocity. The figure shows the maximum real part of the eigenvalues $\Re(\sigma)_{\max} \sqrt{B/g}$ with respect to Froude number F_{n_B} . We kept the beam length B constant. Thus, Froude number is essentially a non-dimensionalized speed. In the towing tank experiment, divergence (porpoising) occurred at about $U = 5.0 [m/s]$ [3] ($F_{n_B} = 3.57$, shown in figure as Experiment) with the nominal l_{cg}/B location of 5.2. Figure 3.3 shows that, in the numerical simulation, planing craft with $l_{cg}/B = 0.50$ turns unstable at just under $F_{n_B} = 5.0$ and with $l_{cg}/B = 0.65$, just under $F_{n_B} = 3.5$. Note that in the physical dimensions, the two l_{cg} values differ only by $0.03 [m]$ (or 1.95% of the float length of $1.54 [m]$ [3]) and the speed limit for stable planing changed by $2.10 [m/s]$ (or 42.8% difference). Thus, the planing speed U at which the craft turns unstable is very sensitive to the CG location. Considering the fact that values for B and l_{cg} are only approximately known, the numerical results are very reasonable in light of the experimental evidence.

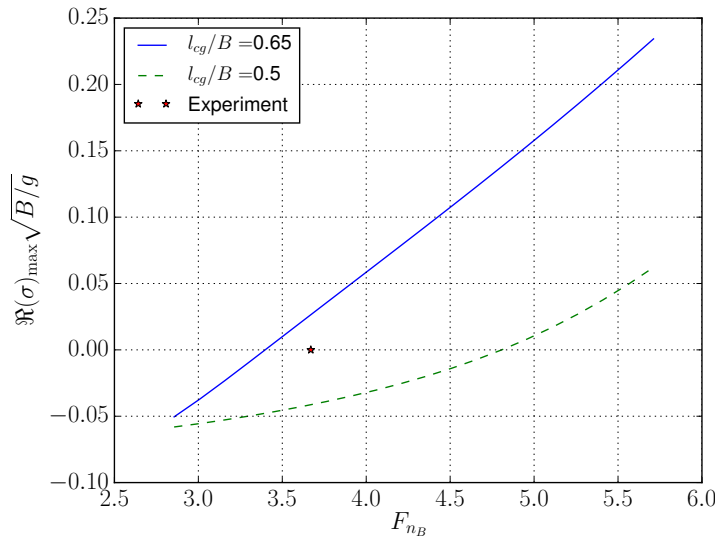


Figure 3.3: Porpoising mitigation by moving the CG aft.

The trim angles τ corresponding to the two l_{cg} values with respect to F_{n_B} are shown in Figure 3.4. The trim angles are found by driving the moment equation

to have near zero residue moment. This is done using Brent's method [33, Ch.3-4] implemented in Scipy optimize module of the Python programming language. One can let the solutions to have small residues so that the trim angles found can be used as a small perturbation in the subsequent eigenvalue computations.

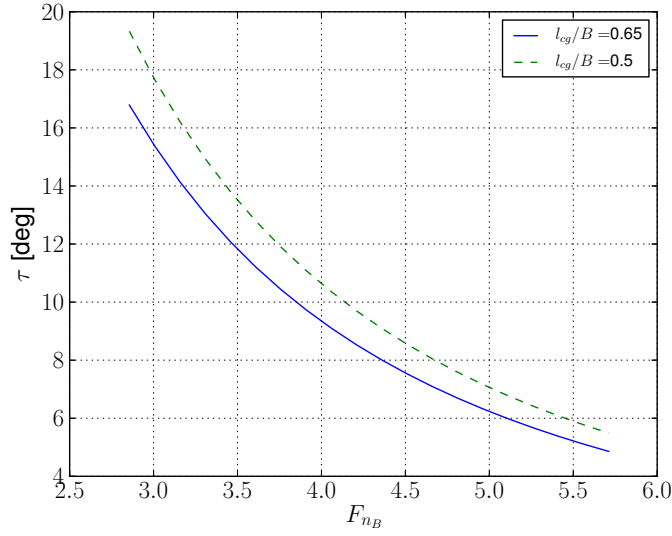
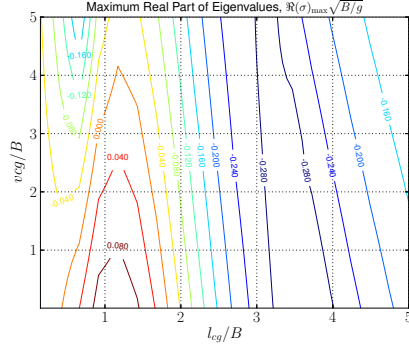


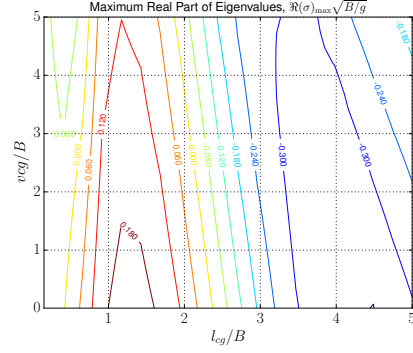
Figure 3.4: Trim angle of the simulated model with respect to Froude number F_{n_B}

Figure 3.5 indicates that the desirable direction of moving the CG ,i.e. forward or backward, to stabilize an unstable planing condition depends on the current value of l_{cg} . There is a band of l_{cg} values at which a non-decaying oscillation manifests with positive $\Re(\sigma)_{\max} \sqrt{B/g}$. This band of instability increases in width as F_{n_B} increases from 2.86 to 5.71 as seen in Figure 3.5a to Figure 3.5e. This qualitatively agrees with the experiment in that the instability happens above certain speed limit, which was 5 [m/s] in the tow-tank experiment. The contour plots show that the sensitivity of the stability to changes in v_{cg} is not as marked as changes in l_{cg} . A small portion of the design space near the transom or very small value of l_{cg} generates stable designs, and most float planes have this configuration to facilitate the pitch up at the moment of take off. This means that to make the planing stable, it is a good idea to shift the CG aft. However, once airborne, it is better to have CG forward to have enough “static margin” for a stable flight.

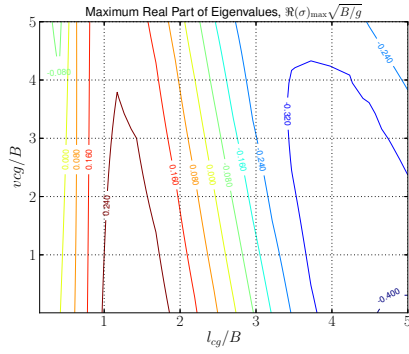
Chapter 3 Results



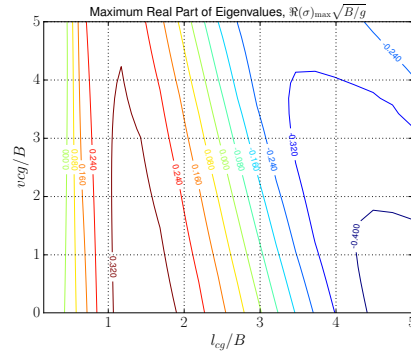
(a) $F_{n_B} = 2.86$



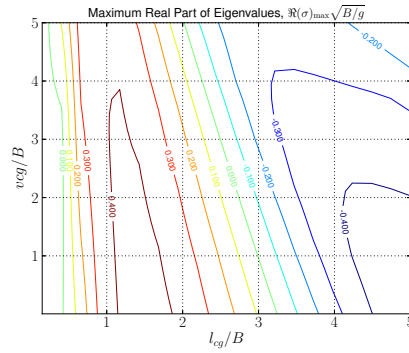
(b) $F_{n_B} = 3.57$



(c) $F_{n_B} = 4.28$



(d) $F_{n_B} = 5.00$



(e) $F_{n_B} = 5.71$

Figure 3.5: Stability with respect to l_{cg} and v_{cg} . $\Re(\sigma)_{\max} \sqrt{B/g} < 0$ are stable designs.

3.2.1. Conclusion of Rigid-Support Case

The rigid-support simulations demonstrate that there is a satisfactory match between the experimental observation and the numerical model in terms of the effect of the CG location to the longitudinal stability. Qualitatively, there was a match to the fact that, in both the experiment and the numerical model, the stabilizing direction of movement of the CG was backward, towards the step, i.e. decreasing l_{cg} . Quantitatively, the experiment and the numerical model agree to within 3 centimeters (1.95 % of float length) on CG location l_{cg} and to within 42.8 % on Froude number F_{nB} of Porpoising. Since Porpoising is apparently very sensitive to the longitudinal location of CG, the numerical model was considered to be fairly accurate.

A possible cause of inconsistency in the literature regarding the stabilizing direction of movement of the CG has also been identified. In the longitudinal direction along the keel, there is a band of CG locations at which the craft is unstable. Depending on the location of CG relative this band the stabilizing direction of moving CG is different. This band of instability is a function of F_{nB} and tends to widen as F_{nB} increases. This also explains how a stable planing craft at low planing speed turns unstable as the planing speed is increased.

3.3. Flexible-Support Case

Figure 3.6 checks whether the two simulation codes, one for the rigid-body case and the other for the flexibly supported case, agree if the flexible support's spring were extremely stiff. The plot shows $\Re(\sigma)_{\max} \sqrt{B/g}$ with respect to F_{nB} . The two lines agree very well.

In the experimental data shown in Figure 3.2 it was seen that flexible support is capable of suppressing porpoising. Figure 3.7 - Figure 3.9 show computationally the effectiveness of the flexible support in mitigating unstable oscillations. However, as can be noted from the sharp rise in the real part of eigenvalues at high Froude numbers, it is not a globally stabilizing solution. Inadequate damping in the flexible supports can worsen the stability of the seaplane compared with the conventional rigidly supported ones as seen in Figure 3.7a or in Figure 3.7b. This suggests that

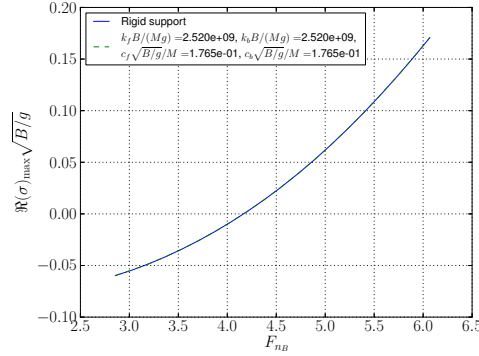


Figure 3.6: Comparison of stability results in the rigid-body formulation and the flexible-support formulation with very stiff springs

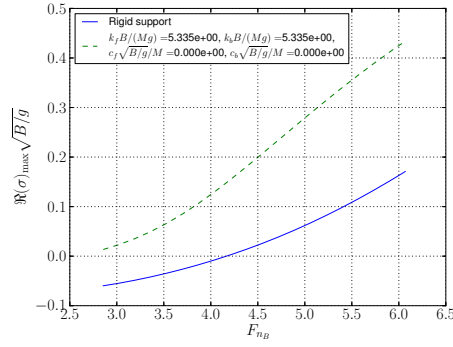
the damper should be designed carefully in such a way that no divergent oscillation modes occur in the planing speeds of the aircraft. Figure 3.8 shows that if only one of either front or back support is made flexible, it is the back support that is effective in mitigating instabilities. Similarly, if damping is applied to either the front or the back support (that are both flexible), it is the damping of the back support that is more effective (Figure 3.9). These results show some similarity with the flutter stability phenomena in Aeroelasticity, in which the elastic axis location of the wing affects the divergence speed.

3.3.1. Conclusion of Flexible-Support Case

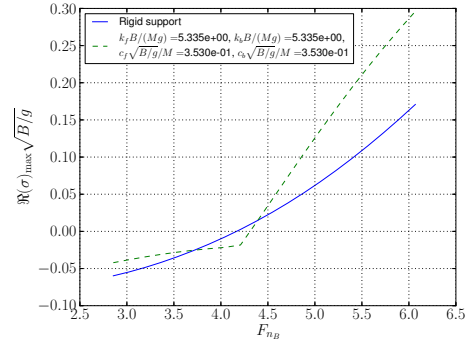
The results in this section showed two things. First, it demonstrated that the model gave identical longitudinal stability to that of the rigid-support case when the flexible support was set to be extremely stiff. Thus, the two numerical models are consistent. Second, it showed that flexible support could have a substantial stabilizing effect depending on the values of spring constant and damping. This is in line with what was observed in the tow-tank experiment. The numerical model showed that the damping coefficient plays an important role in the planing speed at which the craft becomes unstable.

The computational results show that there is a difference in stability if only the front or the back side of the supports is made flexible without damping. The

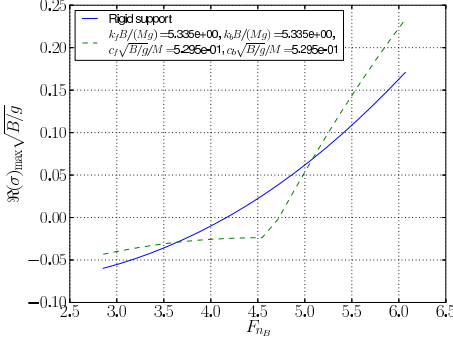
3.3 Flexible-Support Case



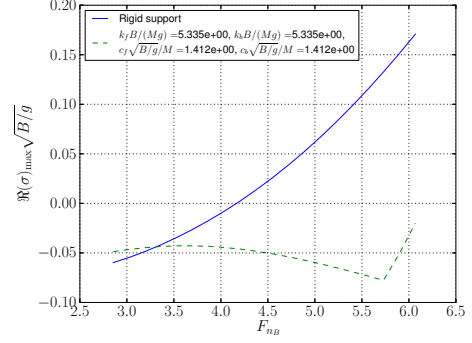
(a) No damping



(b) $c_{f,b} = 20$ [N s/m]



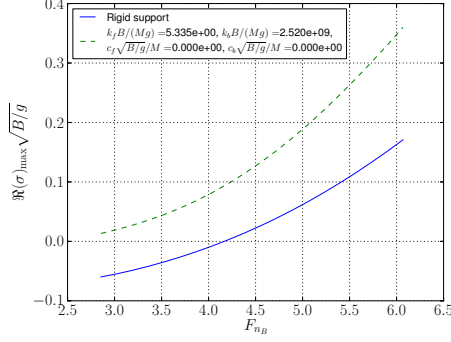
(c) $c_{f,b} = 30$ [N s/m]



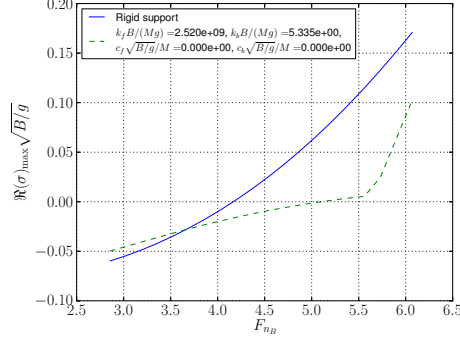
(d) $c_{f,b} = 80$ [N s/m]

Figure 3.7: Comparison of longitudinal stability between rigidly supported case and flexibly supported case. Fixed spring constant $k_{f,b} = 2117$ [N/m] with various damping coefficients.

Chapter 3 Results

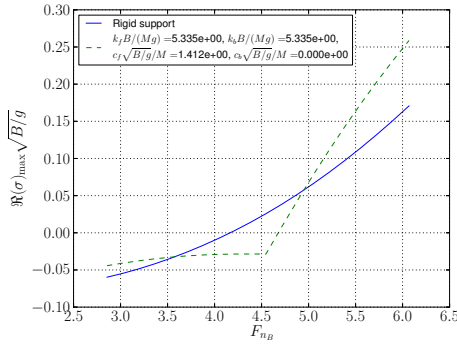


(a) Flexible front support, no damping

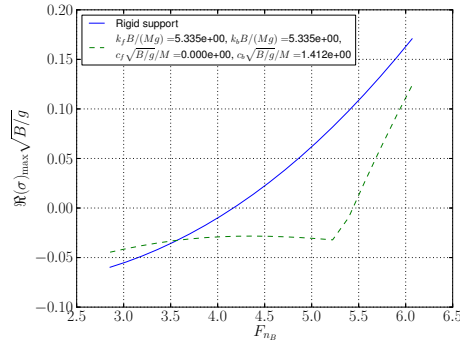


(b) Flexible back support, no damping

Figure 3.8: Comparison of longitudinal stability between the rigidly supported case and the flexibly supported case. Spring applied only to the front k_f or to the back k_b , with no damping applied



(a) Applying damping only to the front support



(b) Applying damping only to the back support

Figure 3.9: Comparison of longitudinal stability between the rigidly supported case and the flexibly supported case. Fixed spring constant $k_{f,b} = 2117[N/m]$, with damping of $80[N s/m]$ applied to either the front or the back support

flexible back-side support has a stabilizing effect, whereas the flexible front-side support alone has a destabilizing effect. Likewise, if both the front and the back support are flexible but only one of them has a damper, the one with a damper on the back-side support has a higher planing speed limit before it becomes unstable (under the condition that both sides had the same spring stiffness coefficients, i.e. $k_f = k_b$). In the following sections, we look further into the relationships between the longitudinal stability and the design parameters.

3.4. Oscillation Analysis

To understand the actual oscillation that is happening, root-loci and time histories of oscillations are plotted. In Figure 3.10, eigenvalues of the system matrix \mathbf{K} of equations 2.1 and 2.2 as described in section 3.2 are plotted for 20 different values of F_{nB} , from 2.856 to 6.068. The flexible-support configuration used in the plot was $k_{f,b}B/(Mg) = 5.335$ and $c_{f,b}\sqrt{B/g}/M = 0.5295$. The vertical axis denotes the imaginary component and the horizontal axis denotes the real component of the eigenvalues. The symmetry with respect to the real axis is due to the fact that the oscillating roots come in complex conjugate pairs. The rightmost oscillation modes going to positive values in the real components are the unstable diverging modes. Figure 3.11 plots the same support configuration as above but up to $U = 14.2$ [m/s] or $F_{nB} = 10.138$ (with $B = 0.2$ [m]) at which point the calculation fails due to dry chine. The extended root-locus plots of Figure 3.11 indicates that the diverging oscillation subsides again at much higher planing speed. The corresponding results for different configurations of flexible supports are given in Appendix C. Figure 3.12 and Figure 3.13 show the time histories of the oscillations of the rigid-support case's and the flexible-support case's state variables respectively for the same configurations shown in the root-locus plot Figure 3.10. They show, in vertical axes, the oscillation of pitch (subscript 5) in radians and of heave (subscript 3) in meters. The horizontal axes are time in seconds. Time histories of four different speeds around the stability limit are shown in both cases. To initiate the oscillation, a perturbation of +5 degrees was given to the pitch attitude from the equilibrium

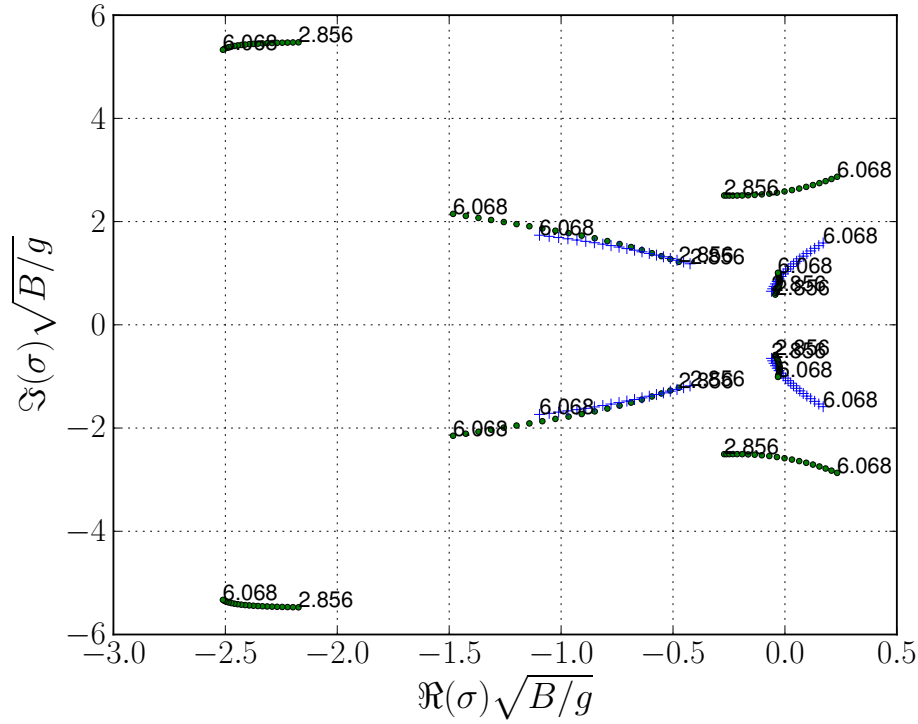


Figure 3.10: Root-locus plot of Figure 3.7c. The cross dots are for the rigid-support case and the round dots are for the flexible-support case. The number beside the dots indicate Froude numbers F_{nB} .

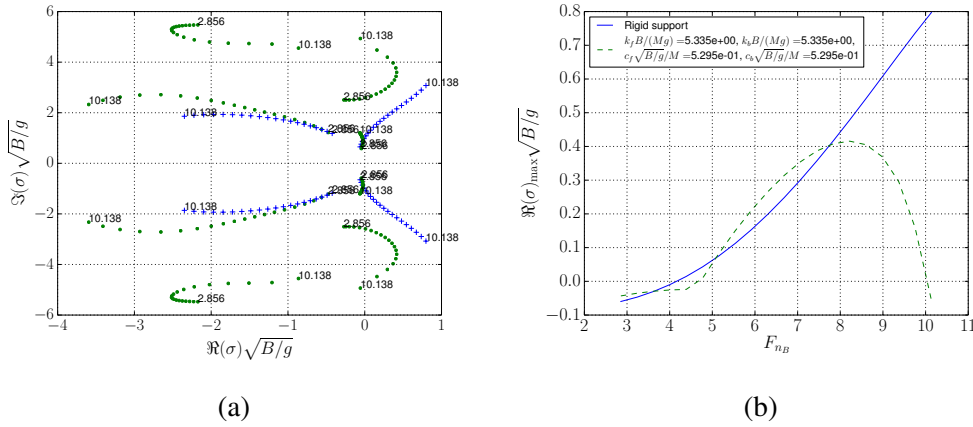


Figure 3.11: Root-locus and $\Re(\sigma)_{\max}\sqrt{B/g}$ plot of Figure 3.7c extended to higher Froude number $F_{nB} = 10.138$ or $U = 14.2$ [m/s] ($k_{f,b} = 2117$ [N/m], $c_{f,b} = 30$ [N s/m])

3.4 Oscillation Analysis

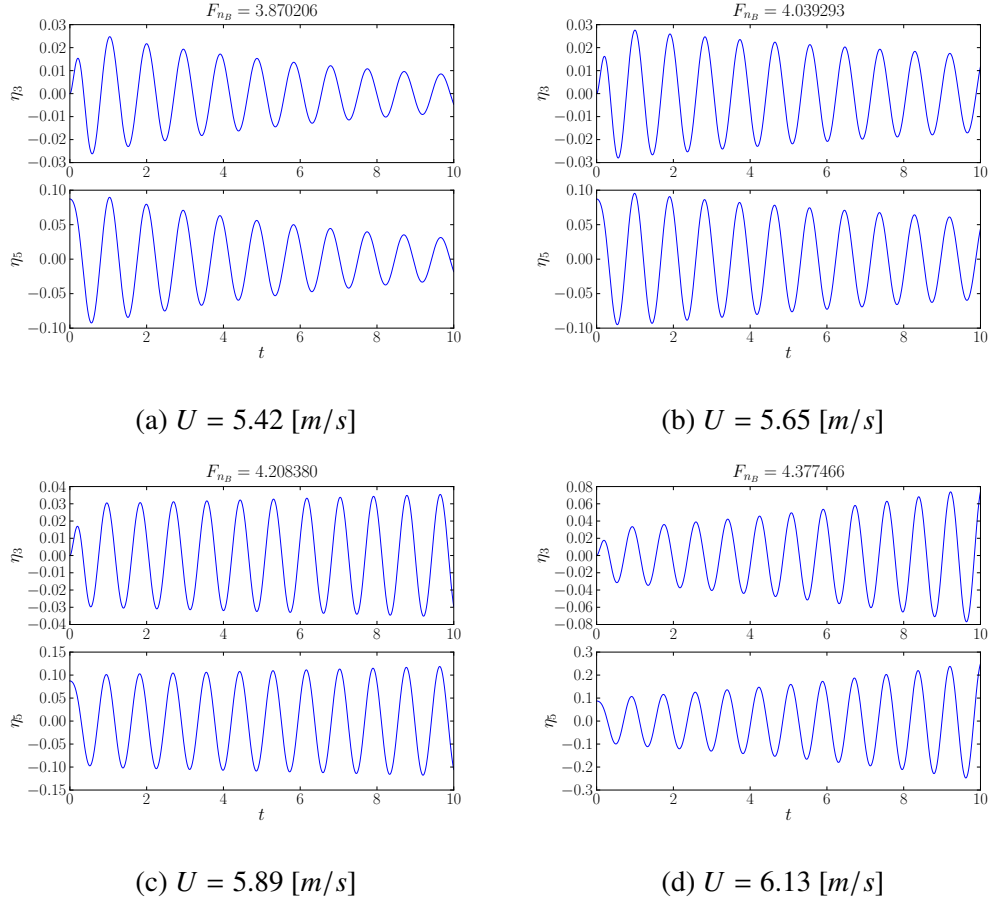


Figure 3.12: Time histories of heaving and pitching oscillations of the rigid-support case at different F_{nB}

position. The rigid-support simulations show that pitch and heave are almost in phase. This is consistent with the experiment data given in Figure 3.2a.

The oscillation of the flexible-support case is more complex. As seen from the root-locus plot Figure 3.10, there are two oscillation modes that are slow to decay and one of them, with shorter period, can diverge if the planing speed (or F_{nB} in the plot) gets high enough. Figure 3.13 shows this situation in time domain. The higher frequency component of the oscillation becomes more prominent as the planing speed increases. In this roughly twice higher frequency than the other one, pitching of the craft ξ_5 and the float η_5 are near 180 degrees out of phase. On the other hand, heaving motions ξ_3 and η_3 are in phase. This is reminiscent of a rodeo riding in which the cowboy pitches down when the bull pitches up and vice versa while they

Chapter 3 Results

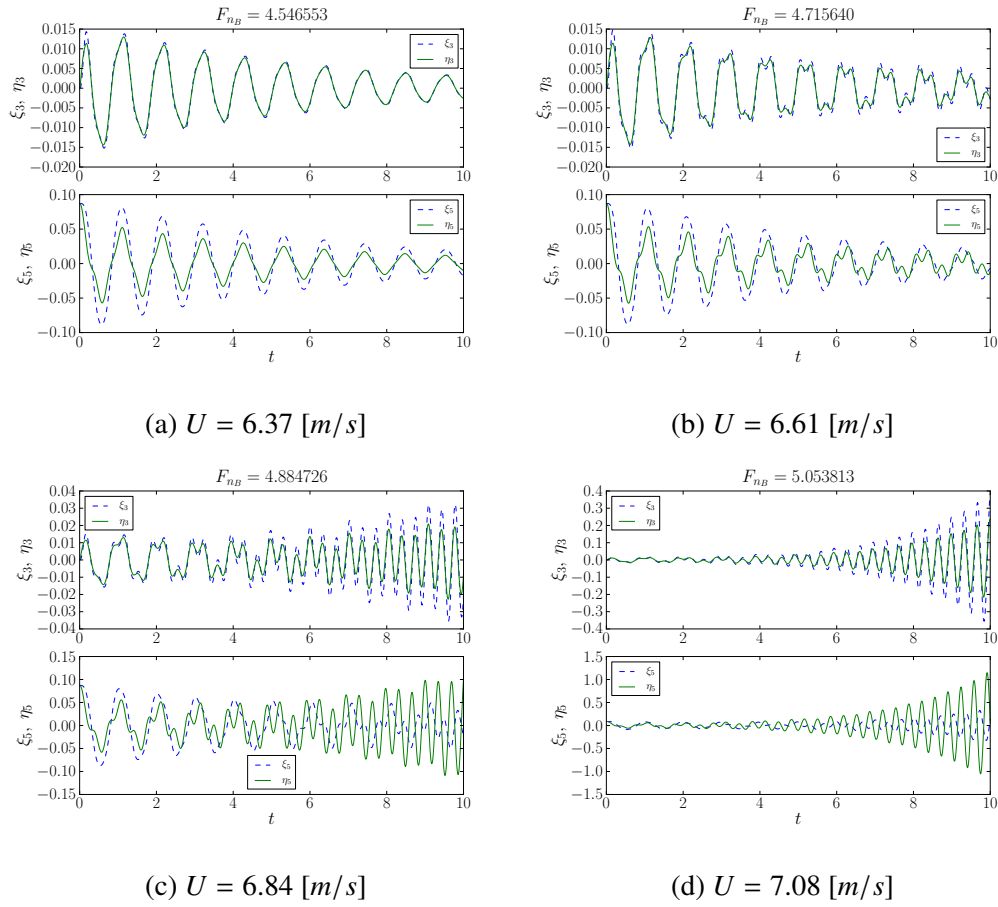


Figure 3.13: Time histories of heaving and pitching oscillations of the flexible-support case at different F_{n_B}

3.4 Oscillation Analysis

almost coincide in the heaving motion. This phenomenon has not been observed in a experiment yet, and must be investigated in the future. This is particularly important since the computational results suggests that the destabilization happens much more quickly with respect to increase in planing speed in the flexible-support case (Figure 3.13) than in the rigid-support case (Figure 3.12).

To see the phase differences between the state variables in the slowest-decaying or diverging oscillation modes, Figure 3.14 and Figure 3.15 show the eigenvectors' components in polar plots. Four different planing speeds are shown. In Figure 3.14 we see that the angles between $\dot{\eta}_3$ and $\dot{\eta}_5$ are small.

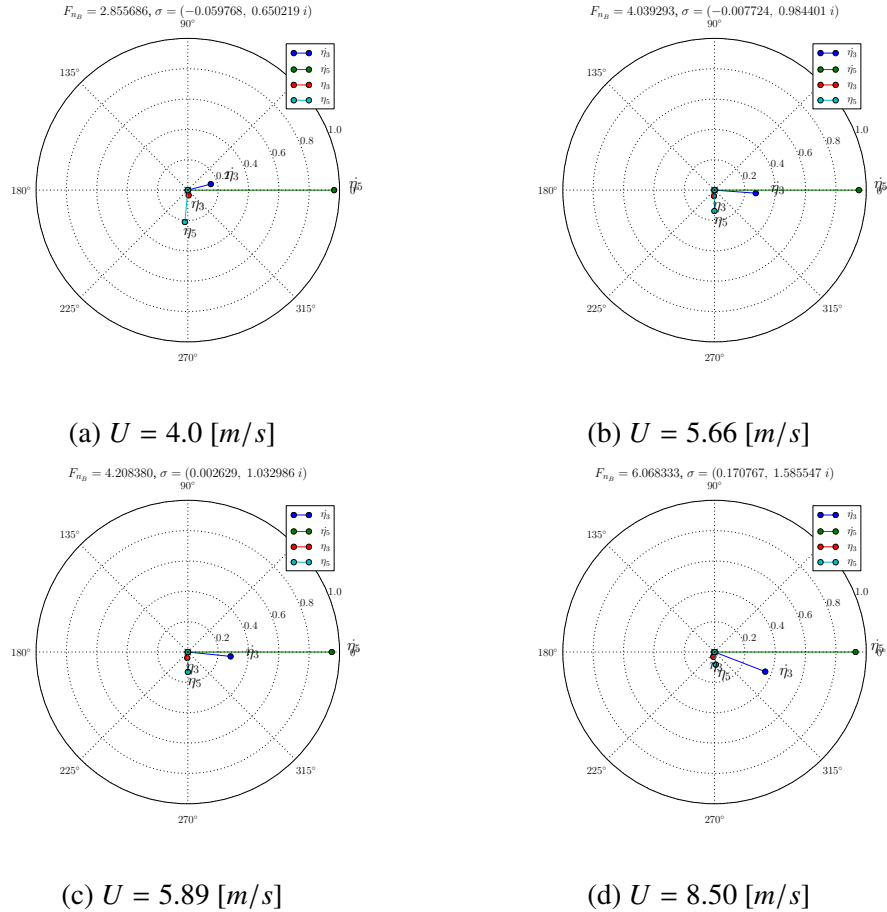


Figure 3.14: Argand plots of eigenvectors corresponding to $\Re(\sigma)_{max}$ of the rigid-support case at different F_{n_B} . The eigenvectors' magnitudes are normalized to one.

In the flexible-support case, the oscillation mode is similar to those of rigid-support case at low speed as seen in Figure 3.15a. Both the float and the upper

Chapter 3 Results

structure (the craft), as well as their heave and pitch, are in sync with very small phase differences. At higher speeds, Figure 3.15b-Figure 3.15d, a different oscillation mode with large phase difference (close to 180 degrees) in pitch ξ_5 and η_5 takes the place of $\Re(\sigma)_{max}$.

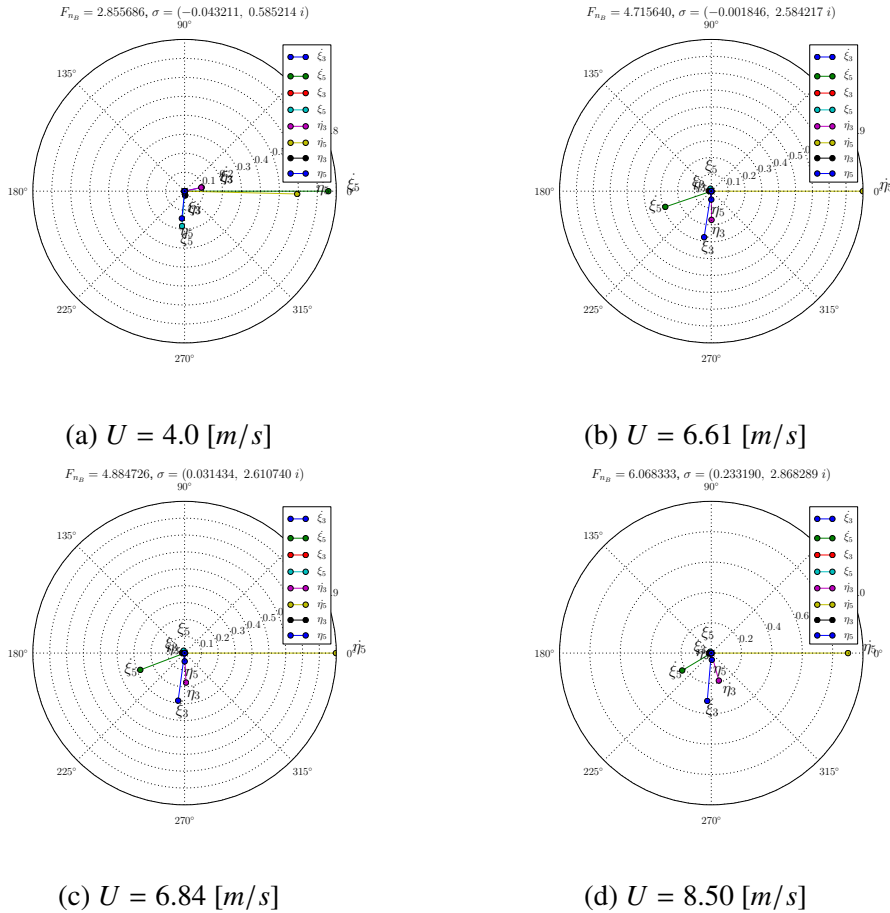


Figure 3.15: Argand plots of eigenvectors corresponding to $\Re(\sigma)_{max}$ of the flexible-support case at different F_{nB} . The eigenvectors' magnitudes are normalized to one.

3.4.1. Conclusion of Oscillation Analysis

The oscillation analysis revealed that there were two oscillation modes that were slow to damp out in the flexible-support case. One is Porpoising, and the other is an oscillation between the upper structure and the floats that has almost 180 degrees phase difference in the pitching. The kink observed in $\Re(\sigma)_{max}$ vs. F_{nB} plots are due to the switch in oscillation modes providing the $\Re(\sigma)_{max}$ values. It is also observed

in the numerical results that the pitching and the heaving of porpoising are almost in phase. This was also the case with the time histories of measurements from the tow-tank experiment of the rigid support case.

Although the flexible support suppressed porpoising by a judicious choice of spring and damping coefficients, the other oscillation mode could diverge at higher planing speed. This is a resonance phenomenon and the oscillation can become stable again at even higher planing speed. However, there is an upper limit to the speed the numerical model can simulate as the draft of the hull can become too shallow.

3.5. Sensitivity Analysis

In this section, the effect of changes in design variables on the planing speed at which the craft turns unstable is investigated. We denote the stability limit speed as U_{lim} . Additionally, the effect of changes in design variables on the maximum value of the real part of the eigenvalues $\Re(\sigma)_{max}$ given a planing speed U is also investigated. The two linear models are used to estimate the U_{lim} via the root finding algorithm, Brent's method [33, Ch.3-4]. This is done by finding the U at which $\Re(\sigma)_{max}$ turns zero. In this section and in the next, the dimensional quantities are shown instead of the nondimensional ones as the scaling parameter B changes and not convenient for the interpretation of the sensitivity.

To see the sensitivity of U_{lim} with respect to the design variables, we perturb the design variables from the nominal values. For the rigid support, they are l_{cg} , vcg , B , β_{deg} , I_{55} , f , ϵ . For the flexible support, they are l_{cg} , vcg , B , β_{deg} , I_A , I_B , f , ϵ , k_f , k_b , c_f , c_b . We sample randomly and uniformly between upper and lower bounds. The bound are set such that they are $\pm 10\%$ of the nominal values except for $\epsilon = 0 \pm 2$ [deg] and $f = 0.00 \pm 0.05$ [m]. Note that, larger nominal values results in larger difference between upper and lower values when proportional bounds such as $\pm 10\%$ are applied. It is important to bear this fact in mind when interpreting a global sensitivity analysis. The nominal values for spring and damping are set to $k_{f,b} = 2117$ [N/m] and $c_{f,b} = 40$ [N s/m] respectively. The $c_{f,b}$ are chosen in such

Chapter 3 Results

a way that the damping ratio is $0.2 < \zeta < 0.8$ in one-dimensional representation of the flexible model, following the usual range for automobile [34]. The damping ratio is defined as

$$\zeta = \frac{c}{2\sqrt{M \cdot k}}, \quad (3.1)$$

where, in our case, $c = c_f + c_b = 40 + 40 [N \cdot s/m]$, $k = k_f + k_b = 2117 + 2117 [N/m]$, and $M = m_A = 10.79/2 [kg]$ obtained from the half body representation. Then, $\zeta = 0.265$.

In Figure 3.16, the effects of the perturbation of the design variables on the value of U_{lim} are shown. The figure shows the results of 3000 uniform random samples.

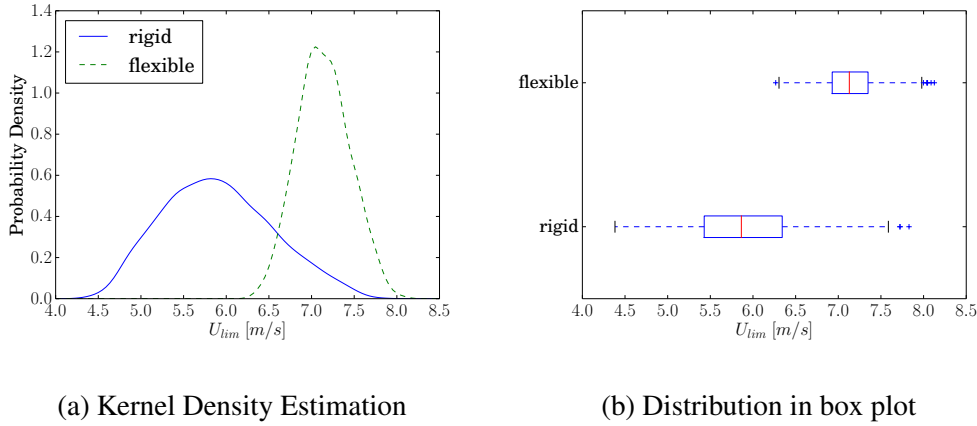


Figure 3.16: Distribution of U_{lim} due to design variable changes within $\pm 10\%$ of nominal values

To measure the influence of each of the variables, total effect indices are used [35, 36]. Let $y = f(\mathbf{x})$ a deterministic function where \mathbf{x} is a vector of input variables whose element is denoted by x_i and the other elements not x_i as \mathbf{x}_{-i} . The total effect of an input variable x_i to output y is

$$S_{T_i} = \frac{E_{\mathbf{x}_{-i}}(V_{x_i}(y|\mathbf{x}_{-i}))}{V(y)} = 1 - \frac{V_{\mathbf{x}_{-i}}(E_{x_i}(y|\mathbf{x}_{-i}))}{V(y)}, \quad (3.2)$$

where E_{x_i} denotes the mean due to changes in x_i and V_{x_i} means variance due to changes in x_i . The computation of equation (3.2) is done using Jansen's method [37]. The $E_{\mathbf{x}_{-i}}(V_{x_i}(y|\mathbf{x}_{-i}))$ tells you the expected variance in output y when all inputs except x_i are fixed (and you have to fix at m many different values of \mathbf{x}_{-i} to get the expected

3.5 Sensitivity Analysis

variance of y due to changes in x_i). Thus, S_{T_i} shows its proportion in relation to unconditional variance $V(y)$ such as in Figure 3.16. The total cost for obtaining the S_{T_i} is $m(k+2)$ function evaluations where m is the number of random samples and k is the number of input variables. Figure 3.17 shows the S_{T_i} of the rigid and flexible

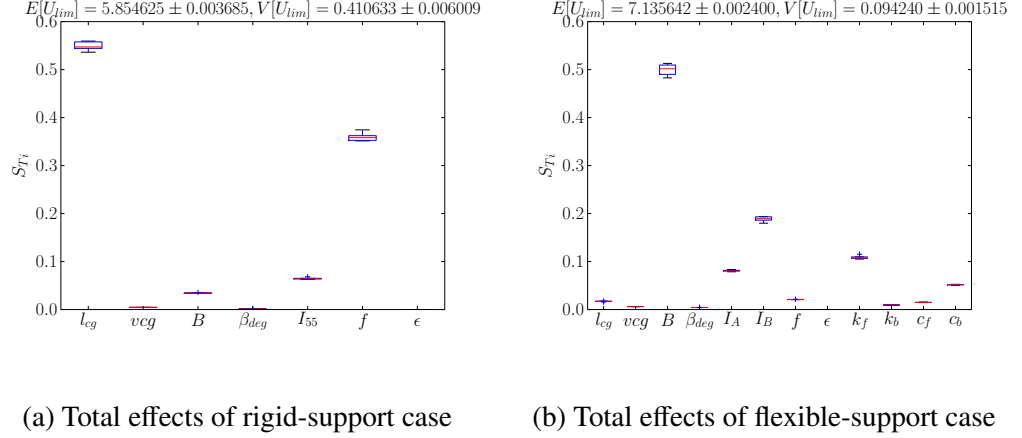


Figure 3.17: Total Effect of each design variables

case design variables. The computation was done with $m = 3000$ and $k = 7$ for the rigid and $k = 12$ for the flexible case. Five replicates were performed with the same settings to get an idea of the precision of the indices which are indicated by the box plot in the plot and the standard deviation values for average and variance of U_{lim} (shown at the top of the plots).

Figure 3.17a shows that the most influential variable in the rigid-support case is l_{cg} , followed by f and I_{55} . On the other hand, Figure 3.17b shows that, in flexible-support case, B is the most influential followed by I_B , k_f , and I_A . Note that $V[U_{lim}]$ is four times bigger for the rigid-support case than the flexible-support case. The existence of the flexible support absorbed some of the variation of U_{lim} and shifted its average to higher values (i.e. from 5.85 to 7.14 [m/s]). Considering the fact that standard deviation of U_{lim} in rigid-support case is $\sqrt{0.41} = 0.64$ [m/s], the increase of U_{lim} , $7.14 - 5.85 = 1.29$ [m/s] is quite significant.

Figure 3.18 to Figure 3.20 show the sensitivities of the rigid and flexible support design variables to the maximum values of the eigenvalues $\Re(\sigma)_{\max}$. The upper and lower bounds of the design variables stay the same as in the sensitivity analysis U_{lim} .

Chapter 3 Results

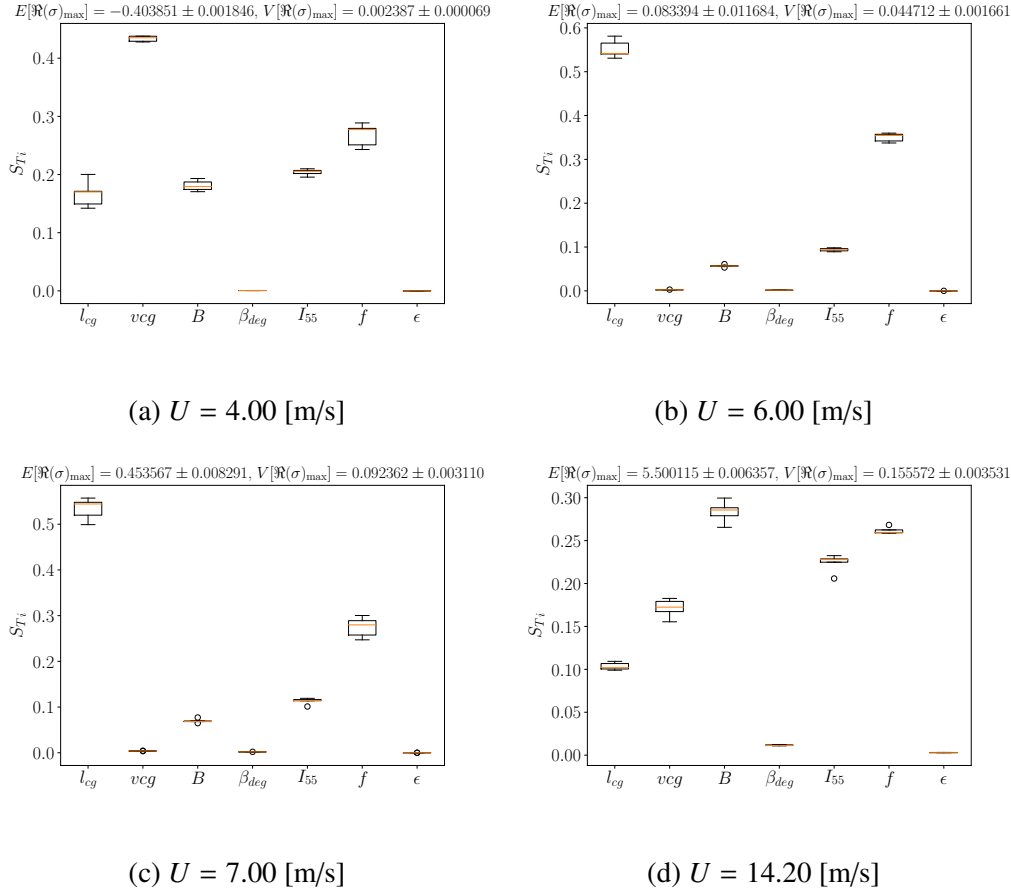


Figure 3.18: Total Effect of each design variables on $\mathfrak{R}(\sigma)_{\max}$, rigid-support case

However, now the planing speed U was fixed at 4.00, 6.00, 7.00 and 14.20 [m/s] respectively. This time, m was set to 1000, and 5 replicates were done to get the box plots. Through these plots, it is possible to see that the relative importance of the design variables affecting $\mathfrak{R}(\sigma)_{\max}$ changes depending on the planing speed.

At $U = 4.00$ [m/s], in Figure 3.18a and Figure 3.19a, the vertical position of the center of gravity vcg is the most important for the variance of $\mathfrak{R}(\sigma)_{\max}$ in both rigid and flexible support cases. In the rigid body case, it is followed by the pitch up moment arm length of the thrust line f . In the flexible body case, it is followed by the aircraft moment of inertia I_A . The flexible-support case, in general, has bigger $\mathfrak{R}(\sigma)_{\max}$ than that of the rigid-body case as seen in Figure 3.20a. At this speed, no combination of design variables within the bounds was shown to be unstable in both rigid- and flexible-support cases.

3.5 Sensitivity Analysis

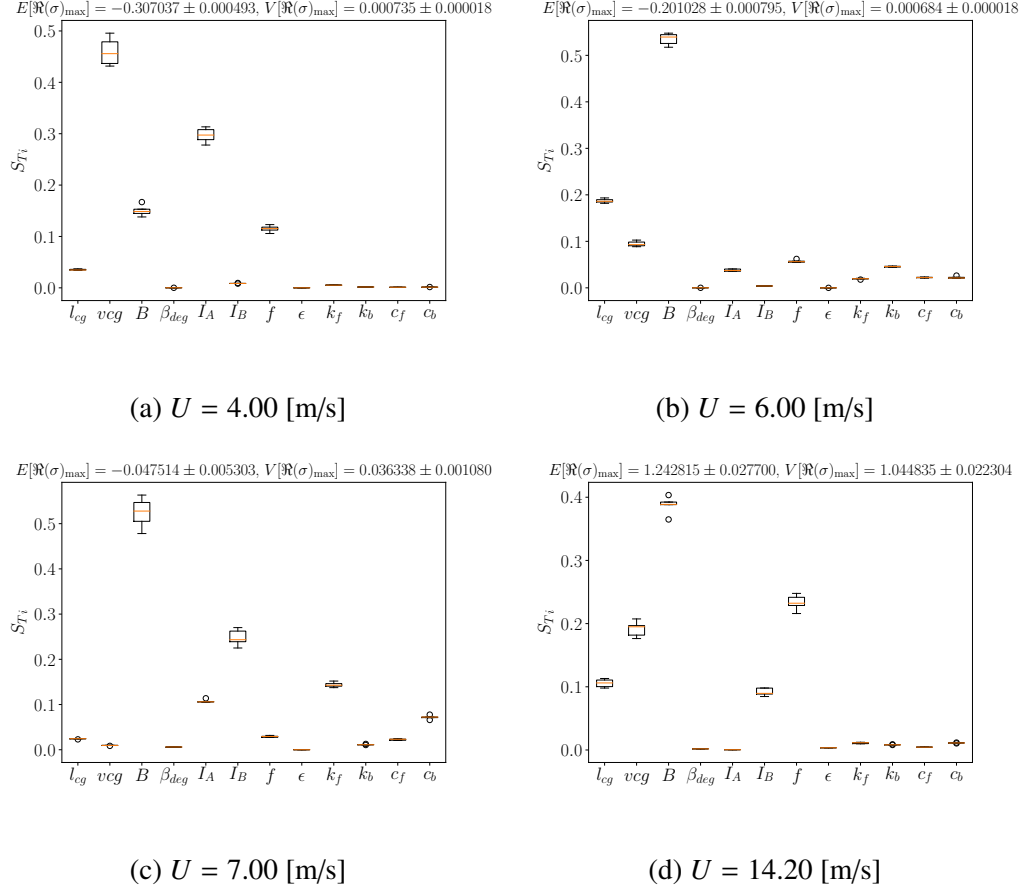


Figure 3.19: Total Effects of each design variables on $\Re(\sigma)_{\max}$, flexible-support case

At $U = 6.00$ and 7.00 [m/s], in Figure 3.18 and Figure 3.19, the most important variable becomes the longitudinal location of the center of gravity l_{cg} in the rigid-support case and the beam length B in the flexible-support case. On average, rigid-support designs are unstable but flexible-support designs are stable at these speeds.

At $U = 14.20$ [m/s], however, B becomes the most influential variable for both the rigid-support and the flexible-support cases. Another aspect at this speed is that f becomes the second most important variable in the flexible-support case whereas, in the other three slower speeds, f ranks in the fourth or lower.

In the four different speeds, $k_{f,b}$ and $c_{f,b}$ are by themselves not the dominant factor as evidenced by the relatively low values of S_{T_i} in Figure 3.19. However, their presence alters the importance of other design variables such as l_{cg} and B when

Chapter 3 Results

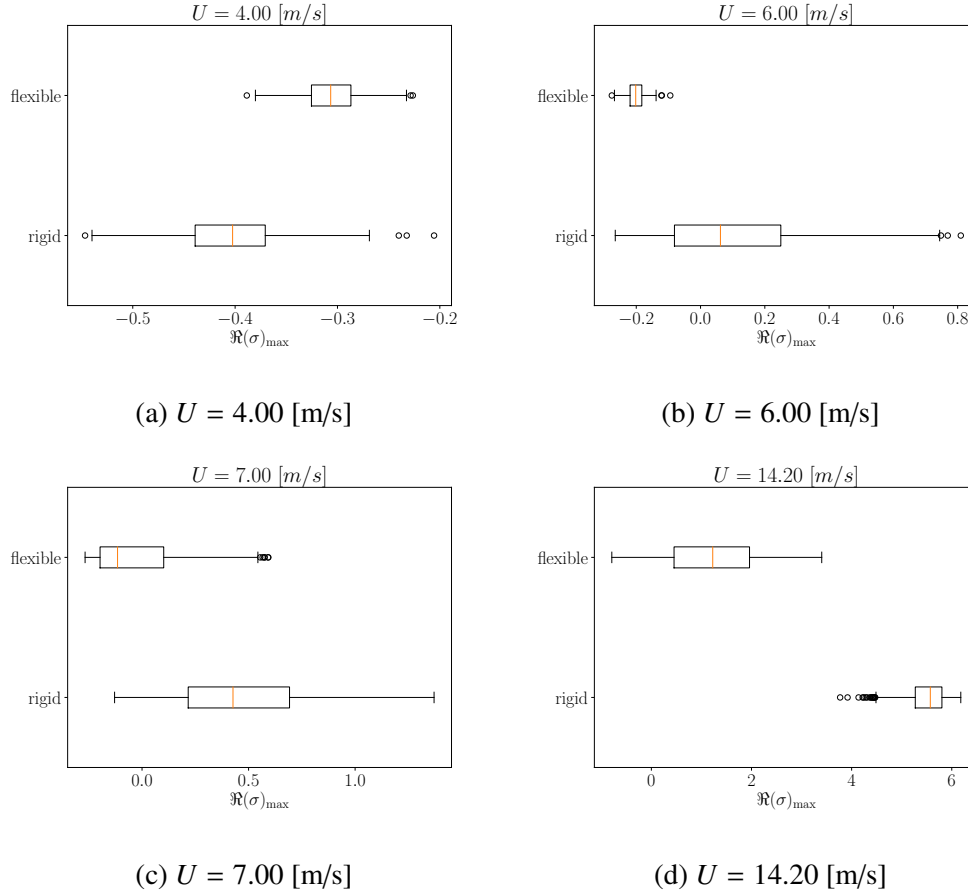


Figure 3.20: Distribution of maximum eigenvalues $\Re(\sigma)_{\max}$ with respect to the variation in the design variables.

compared to those in Figure 3.18. Furthermore, the relative importance of k_f vs. k_b and c_f vs. c_b seems to change depending on the planing speed U .

Figure 3.20 shows the distribution of $\Re(\sigma)_{\max}$ at the four speeds when the design variables were varied as uniform distribution within the upper and lower bounds. Except for $U = 14.20$ [m/s], both rigid and flexible support are capable of generating a stable design. However, the flexible-support case should allow more variety or ease of design as the proportion of stable designs among the random samples is larger than the rigid counterpart. It should be noted that there could be a range of speeds (that were not plotted here) in which the flexible support may not produce any stable design because of the resonance as identified in Figure 3.11. However, this figure indicates that a flexible-support system can provide an effective way to

mitigate porpoising or unstable oscillations.

3.5.1. Conclusion of Sensitivity Analysis

In this section, important design variables affecting the longitudinal stability were identified. On average (median), a significant increase in the stability limit speed U_{lim} was obtained when the rigid support was replaced with the flexible support. The variance of U_{lim} due to the variances of design variables was four times smaller for the flexible support case than for the rigid support case. In the rigid-support case, the U_{lim} was most sensitive to the longitudinal location of the CG l_{cg} , whereas, in the flexible-support case, it was the beam length B .

A for the sensitivity of maximum real part of the eigenvalues $\Re(\sigma)_{max}$, different parameters became important depending on the support case and depending on the planing speed. At the planing speed of $U = 4.0$ [m/s], the vertical position of the CG v_{cg} was the most important for both the rigid and the flexible support. At $U = 6.0$ and 7.0 [m/s], l_{cg} was the most important for the rigid-support case and B for the flexible-support case. At $U = 14.2$ [m/s], the most important variables became B in the rigid-support case, but in the flexible-support case, the most important variable remained to be B .

The variance of the eigenvalues with respect to the design variables showed whether either or both support cases could produce a stable design. At $U = 4.0$, 6.0 , and 7.0 [m/s], both flexible- and rigid-support case were capable of generating stable designs within the design space. However, the chances for a stable design were considerably higher for the flexible support case than those of the rigid-support case. The number of variables simultaneously considered in this study was 7 for the rigid-body case and 12 for the flexible-support case. These numbers are substantially larger compared to what we normally see in the literature of physical experiments of porpoising. This is due to the short execution time of the numerical simulations and computational speed of modern computers.

3.6. Design Subspace Search for Stable Designs

Figure 3.21 shows a contour plot of $\Re(\sigma)_{\max} \sqrt{B/g}$ with respect to l_{cg} and vcg along with sampled points by SOMBAS in two-design-variable case. SOMBAS was set to search feasible designs requiring $\Re(\sigma)_{\max} \sqrt{B/g} < 0$. The sampled points that satisfy that condition are shown along with the final location of the training samples for the Self-Organizing Map (SOM). The distribution of the training samples indicates the finite sample representation of the feasible region around which further sampling in the subsequent iterations is expected to produce further space filling effect of the feasible design space, i.e. further stable designs. In this trivial case (because we already have the contour plot), we see that SOMBAS sampled diverse combinations of l_{cg} and vcg filling out the stable domain. This feasible region search capability is useful when the design space is in higher dimensions (many design variables) and full-factorial design (or grid sampling) becomes too expensive.

Figure 3.22a shows the scatter plot matrix of the seven design variable case. N_f is the number of designs (experiments) computed by SOMBAS and N_s is the number designs that satisfy the condition, i.e., $\Re(\sigma)_{\max} \sqrt{B/g} < 0$. The upper triangular cells show the distribution of point satisfying the stability condition. The design variables forms a multidimensional vector (7 dimensional in this case) and every instance of vectors sampled by SOMBAS that satisfies the stability condition is plotted in the matrix cells. The cells show the two dimensional projection of these vectors. The lower triangular cells show the absolute values of correlation coefficients between given combination of two variables. In sampling, the upper and lower bounds of the design variables were set as follows: $0.03 \leq l_{cg} \leq 1.50$ [m], $0.001 \leq vcg \leq 1.50$ [m], $0.150 \leq B \leq 0.250$ [m], $0.0 \leq \beta_{deg} \leq 20.0$ [deg.], $M \cdot 0.4^2 \leq I_{55} \leq M \cdot 0.8^2$ [kg · m²], $-0.1 \leq f \leq 0.1$ [m], $-3.0 \leq \epsilon \leq 3.0$ [deg.], where $M = 16.18$ [kg] or 8.09 [kg] in half-body representation.

Again, it clearly shows the unstable “band” for l_{cg} at the top row of the scatter plot matrix. Figure 3.23 shows the enlarged view with additional horizontal line drawn to see that there is a certain range of l_{cg} values (cf. see the right margin of the row) for which no stable design was found. Other parameter does not show

3.6 Design Subspace Search for Stable Designs

clear unfeasible regions. Further restriction was applied by setting $\Re(\sigma)_{\max} \sqrt{B/g} < -0.3$ and the results are shown in Figure 3.22b. It shows some new trends. For example (see enlarged view Figure 3.24), vcg tends to lower values as the eigenvalue $\Re(\sigma)_{\max} \sqrt{B/g}$ becomes more negative. On the other hand the beam length B tends to larger values as the eigenvalue $\Re(\sigma)_{\max} \sqrt{B/g}$ becomes more negative. The l_{cg} concentrates between 0.6 and 1.1 (to view ranges of variables, refer to the numbers in the right hand side margin for B and l_{cg} , left hand side margin for vcg , and top margin for $\Re(\sigma)_{\max} \sqrt{B/g}$), and vcg tends to low values as l_{cg} becomes longer (Figure 3.25).

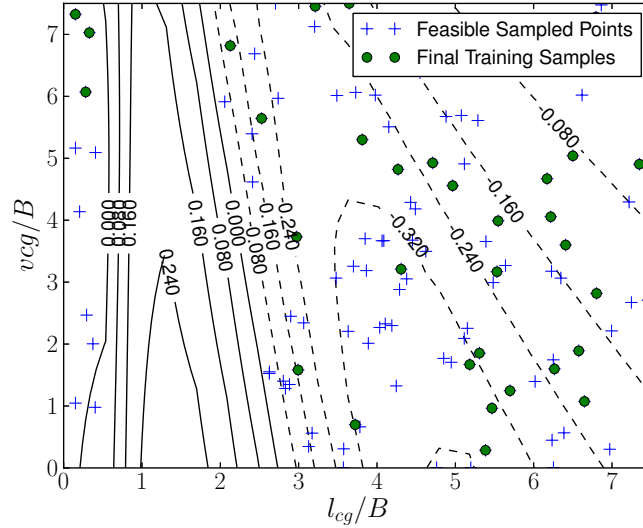
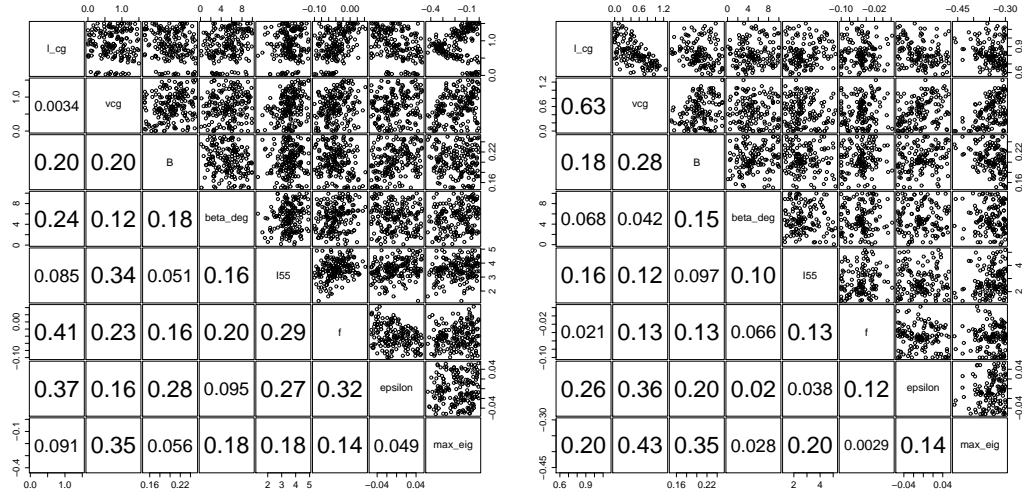


Figure 3.21: SOMBAS sampling stable combinations of l_{cg} and vcg at $U = 6.0$ [m/s]

Figure 3.26 shows the scatter plot matrix of the stable designs, i.e. $\Re(\sigma)_{\max} \sqrt{B/g} < 0$, of the twelve design variable case. The upper and lower bounds of the design variables were set as follows: $0.03 \leq l_{cg} \leq 1.50$ [m], $0.001 \leq vcg \leq 1.50$ [m], $0.150 \leq B \leq 0.250$ [m], $0.0 \leq \beta_{deg} \leq 20.0$ [deg.], $1.958 \leq I_A \leq 2.393$ [$kg \cdot m^2$], $0.7337 \leq I_B \leq 0.8968$ [$kg \cdot m^2$], $-0.1 \leq f \leq 0.1$ [m], $-3.0 \leq \epsilon \leq 3.0$ [deg.], $1905 \leq k_{f,b} \leq 2329$ [N/m], $36.0 \leq c_{f,b} \leq 44.0$ [N s/m], where I_A and I_B are in half-body representation. The most significant feature of the scatter is observed in the top row at the right-hand-side corner, namely the relation between l_{cg} and

Chapter 3 Results



(a) Maximum eigenvalues of oscillation modes less than 0, ($N_f = 289, N_s = 181$) (b) Maximum eigenvalues of oscillation modes less than -0.3, ($N_f = 504, N_s = 135$)

Figure 3.22: Scatter Matrix showing distribution of feasible designs at $U = 6.0$ [m/s]

$\Re(\sigma)_{\max} \sqrt{B/g}$. It is observed that, at least at $U = 6.0$ [m/s], the stability of the craft improves as the location of CG is moved forward, i.e. $\Re(\sigma)_{\max} \sqrt{B/g}$ decreases as l_{cg} increases. However, a more rigorous study should be conducted since $m_{A,B}$, $I_{A,B}$, B_{53} , B_{55} , C_{53} , C_{55} , U , l_{cg} , and vcg are intricately coupled

Figure 3.27 shows the scatter plot for $\Re(\sigma)_{\max} \sqrt{B/g} < -0.15$. The range of l_{cg} satisfying this criteria is confined between 0.5 and 1.1 [m], as can be seen in the top row at the right-hand-side corner, which is narrower compared to between 0.0 and 1.2 [m] in Figure 3.26. Relatively strong correlation between l_{cg} and B is observed. Furthermore, B tends to smaller values as $\Re(\sigma)_{\max} \sqrt{B/g}$ decreases. This is opposite to the tendency observed in Figure 3.24.

3.6.1. Conclusion for Design Subspace Search for Stable Designs

SOMBAS enables us to see possible solutions as a set of discrete point in design space. It can be used to identify relationships among design variables that are not evident from the sensitivity analysis performed in the previous section. The method scales well to high-dimensional design spaces and is suitable to see feasible design

3.6 Design Subspace Search for Stable Designs

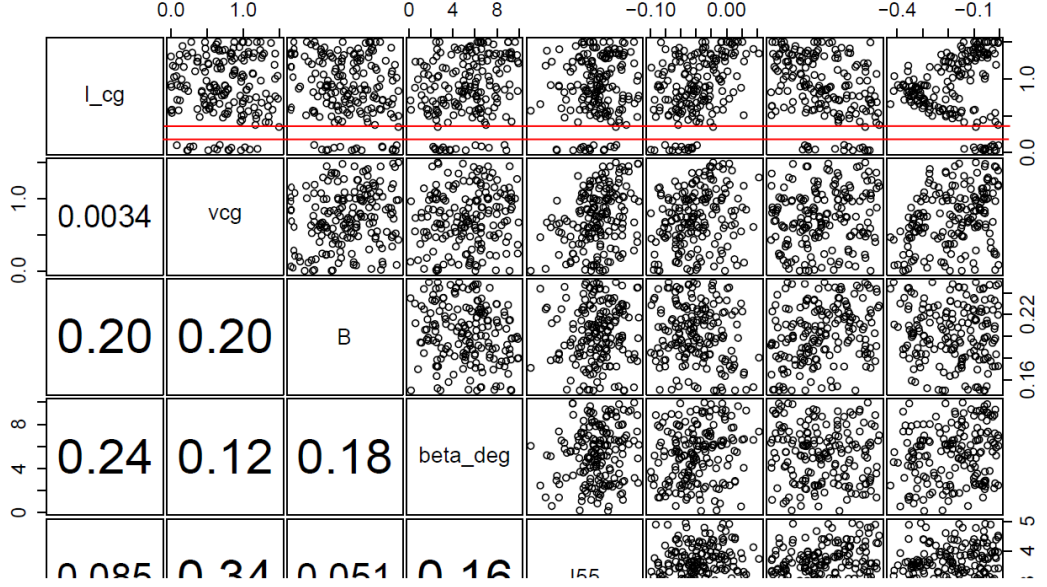


Figure 3.23: The unstable l_{cg} band (from Figure 3.22a).

regions in the design variable spaces.

In this section, some new stability conditions were identified concerning vcg , l_{cg} , B , and $\Re(\sigma)_{\max}$. In the rigid-support case,

- the instability band of l_{cg} was identified.
- for $\Re(\sigma)_{\max} \sqrt{B/g} < -0.3$, vcg tends to lower values as the eigenvalue becomes more negative.
- for $\Re(\sigma)_{\max} \sqrt{B/g} < -0.3$, the beam length B tends to larger values as the eigenvalue $\Re(\sigma)_{\max} \sqrt{B/g}$ becomes more negative.
- for $\Re(\sigma)_{\max} \sqrt{B/g} < -0.3$, l_{cg} concentrates between 0.6 and 1.1 [m].
- for $\Re(\sigma)_{\max} \sqrt{B/g} < -0.3$, vcg tends to low values as l_{cg} becomes longer.

In the flexible-support case,

- the stability of the craft improves as the location of CG is moved forward.
- for $\Re(\sigma)_{\max} \sqrt{B/g} < -0.15$, l_{cg} concentrates between 0.5 and 1.1 [m].
- for $\Re(\sigma)_{\max} \sqrt{B/g} < -0.15$, relatively strong correlation between l_{cg} and B .

Chapter 3 Results

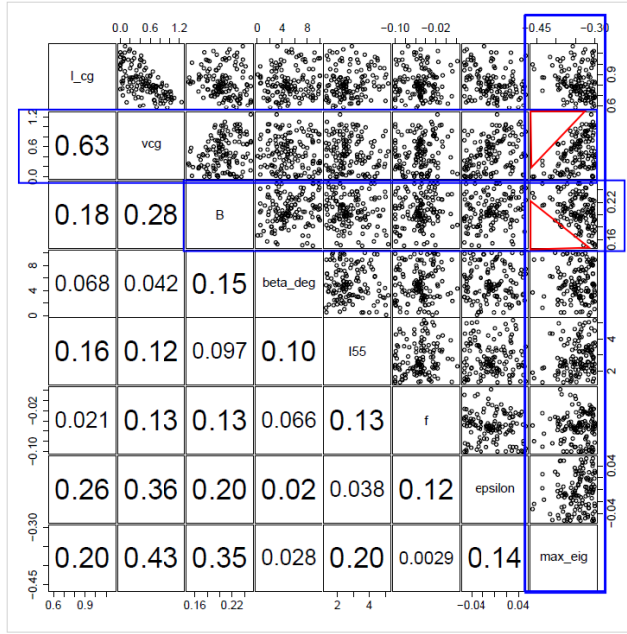


Figure 3.24: vcg vs. $\Re(\sigma)_{\max} \sqrt{B/g}$ and B vs. $\Re(\sigma)_{\max} \sqrt{B/g}$

- for $\Re(\sigma)_{\max} \sqrt{B/g} < -0.15$, B tends to smaller values as $\Re(\sigma)_{\max} \sqrt{B/g}$ decreases.

The reason for the opposite tendency of $\Re(\sigma)_{\max} \sqrt{B/g}$ with respect to B is most likely due to the fact that the pitch-induced added mass of water around the float, A_{55} , A_{53} reduces as B is decreased causing the resonance frequency of the flexible support to be higher, and thus, larger U_{lim} is achieved. On the other hand, in the rigid-support case, damping of pitch motion is only due to B_{53} and B_{55} whose values increases as B increases. However, the trade-off between hydrodynamic damping and the pitch induced mass in determining the stability of the craft is not yet well understood. The interactions among $I_{A,B}$, $m_{A,B}$, β , l_{cg} , vcg , B , $k_{f,b}$, $c_{f,b}$, A_{53} , A_{55} , B_{53} , and B_{55} that affect the resonance frequencies, $\Re(\sigma)_{\max}$ and U_{lim} are quite complex as seen in Appendix A.2 and equation 2.2. Thus, a further study is required to better understand the analytical nature of the planing stability with respect to these variables.

These can form a basis for the next set of physical experiments to see whether such observations as in the lists can be made. Note that the l_{cg} values for $\Re(\sigma)_{\max} \sqrt{B/g} < -0.3$ in rigid-support case and $\Re(\sigma)_{\max} \sqrt{B/g} < -0.15$ in flexible-support case are

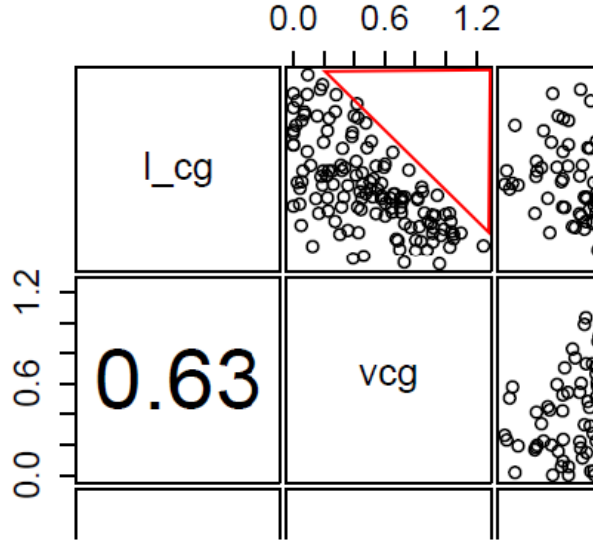


Figure 3.25: l_{cg} vs. vcg (from Figure 3.22b).

too large for a model-float length of 1.54 [m] used in the tow-tank experiments. However, large $\frac{l_{cg}}{B}$ designs (e.g. greater than 2) are a possibility for planing boats and may also be applicable to multi-step planing hulls and innovative designs for seaplanes.

3.7. Parameter Setup for SOMBAS

The parameter values used in obtaining the results in Figure 3.21 and Figure 3.22 are given in Table 3.2. L stands for the value of objective below which diversity of solution is sought. In our case, it corresponds to $\Re(\sigma)_{\max} \sqrt{B/g}$ being 0.0 or some negative values. NT stands for the number of training samples of the SOM algorithm. ρ stands for the weight of diversity enhancing term in the merit function that SOMBAS uses in the selection of new solution candidates. T controls the selectivity of selecting a new candidate solution from SOM and is reminiscent of the Temperature in Simulated Annealing Method. P_{mutation} controls the probability that the selected solution candidate receives a mutation operation. Factors F_e and F_c controls the average magnitude of perturbation in mutation operation. If in the previous iteration a better objective value was found F_e is applied. If it was otherwise, F_c is applied. SOM size controls the number of cells in the map which means

Chapter 3 Results

that it controls the number of new candidate solutions generated in each iteration.

L	ρ	NT	SOM size	T	$P_{mutation}$	F_e	F_c
0.0 or -0.3	0.1	36	6×6	1	1	2.0	0.75

Table 3.2: Parameters setups for SOMBAS

In a general approach to using SOMBAS, the most important parameters are NT and SOM size, These are problem dependent and must be found empirically. In general, if the function is suspected to be more or less smooth like in our case, SOM size of between 3×3 to 6×6 can be chosen and NT of about equal size such as between 9 to 36 can be set up. The other parameters are influential but less critical. For feasible region identification, T would be about 1 or less but larger than say 0.01, and F_e and F_c would have generous expansion and contraction factors as seen in the table. For optimization, T would be set larger value say between 4 and 10. In such a case, F_e would be slightly larger than 1, say around 1.2 and F_c would be equal to or slightly smaller than 1, such as between 0.9 and 1.0.

3.7 Parameter Setup for SOMBAS

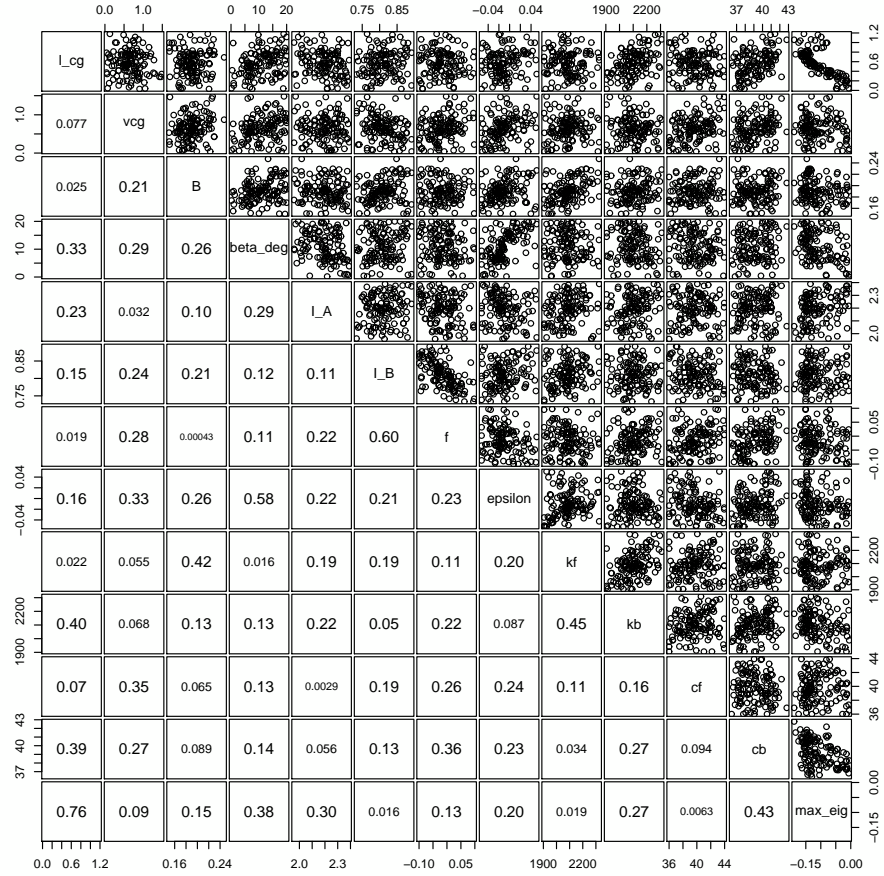


Figure 3.26: Scatter Matrix for the flexible support case with $\Re(\sigma)_{\max} \sqrt{B/g} < 0$ at $U = 6.0 [m/s]$ ($N_f = 140, N_s = 127$).

Chapter 3 Results

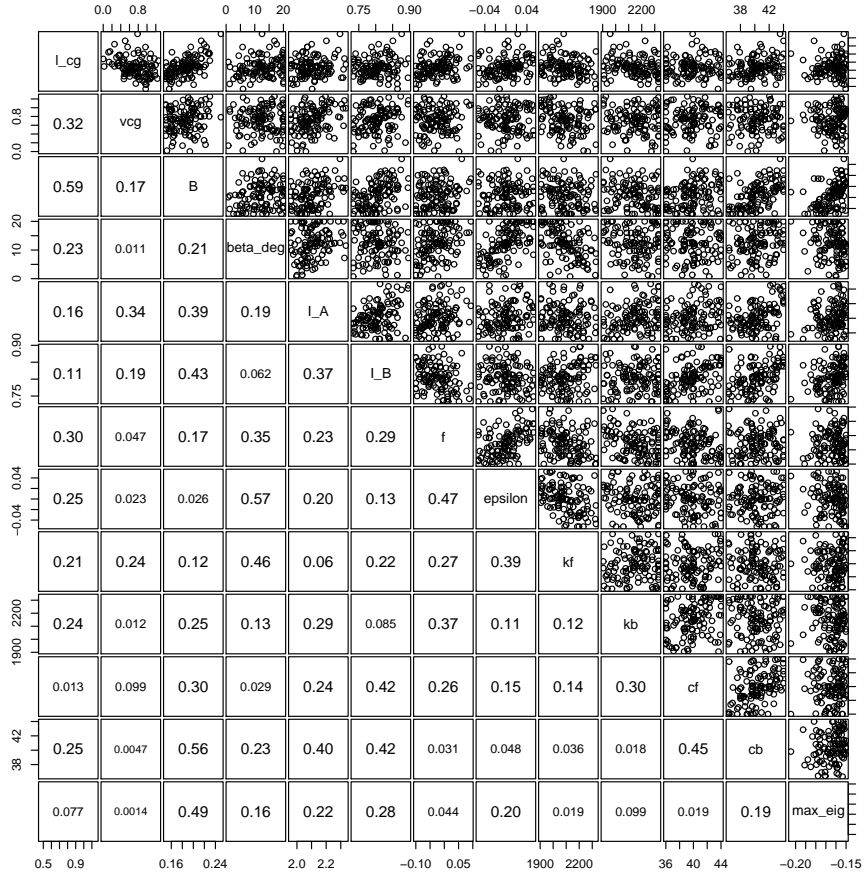


Figure 3.27: Scatter Matrix for the flexible support case with $\Re(\sigma)_{\max} \sqrt{B/g} < -0.15$ at $U = 6.0 [m/s]$ ($N_f = 318, N_s = 113$).

Chapter 4

Conclusion

THE numerical investigation in this research has shown that a flexible-support system for planing craft can effectively suppress porpoising. In the conventional rigid-support configuration, there is an instability band or interval in the longitudinal direction of the center of gravity (CG). This instability band grows wider as the planing speed increases and causes the planing craft to become unstable beyond certain planing speed. In the rigid-support case, this situation can be mitigated by moving the CG aft or forward depending on the location of the CG relative to the instability band. In the flexible-support case, a proper choice of spring constants and damping coefficients has shown to suppress porpoising. However, the flexible support creates a new instability (new resonance frequencies) which can cause instabilities at higher planing speed and oscillation frequency than the original porpoising instability speed. This new instability at higher planing speed is a resonance between the craft and the float with pitch roughly in antiphase and heave almost in sync. The design of flexibly supported seaplanes must ensure that such resonances do not occur in the planing speeds of the aircraft. The search for design variables' values for stable design has been demonstrated using Self-Organizing Map Based Adaptive Sampling (SOMBAS). The feasible set of solutions found by SOMBAS was shown with scatter plots that project the multidimensional design space onto two dimensional spaces via any combinations of two variables. In parametric studies, these plots revealed relationships between two given variables and provided information not directly identifiable in sensitivity studies.

The parametric studies suggest that the longitudinal location of the CG is the most important parameter in determining the stability of the rigidly supported planing craft whereas the beam length of the float is the most important factor in the

flexibly supported planing craft. The scatter plots of SOMBAS' solutions suggest that the instability band does not necessarily exist in the flexible-support case and a stable solution can be obtained with CG location and planing speed that would render the craft unstable in the rigid-support case. Furthermore, under the lower- and upper-bound variables' values, the smaller beam length is favorable for the flexible-support case whereas the opposite is true for the rigid-support case. This is because, in the numerical model, the pitch-induced added mass of water around the float reduces as the beam length is decreased, causing the resonance frequency of the flexible support to be higher. Thus, a larger planing speed without diverging oscillation is achieved. On the other hand, in the rigid-support case, damping of pitch motion is only due to the hydrodynamic damping forces and moments whose values increase as the beam length increases.

The mass of the floats and the longitudinal locations of the front and back flexible support were kept constant. These could be important design variables as they influence the resonance frequencies of the flexible-support system.

It is desirable to conduct further experiments to improve the quality of the model by calibration and further numerical model refinement. The hull geometry and the flexible-support model employed in this research were very simple. The inclusion of the afterbody of the float (the portion after the step) may create another planing surface at larger pitch angles, and this may create another instability. Further sophistication in the flexible-support model, including their control, may render further insights and new opportunities.

4.1. Limitations

The numerical models have been built after the tow-tank experiments and have not been validated by further experiments. It is necessary to further follow up with experiments to verify the predictions made by the model. This process should be iterated to improve the quality of the numerical models.

In the current study, the CG location (l_{cg} and vcg) and the pitching moment of inertia ($I_{55}, I_{A,B}$) was treated independently. However, in reality, they are not. If you

change the CG location, so do the moments of inertia. Thus, care must be taken to interpret the results in this paper where both variables are treated independently.

In this work, the aerodynamic effects were not considered. However, seaplanes receive substantial lift force at planing speeds and the elevator provides a means to control the pitch angle. Thus the aerodynamics may have a substantial effect on the planing characteristics of a seaplane. The inclusion of the aerodynamic effects will be the next step in the development of the numerical simulation of the planing seaplanes.

4.2. Contributions

Followings are the contributions of this thesis.

- Derived a linear-time-invariant model for the flexible-support system for the planing seaplane.
- Investigated high-dimensional design variable space to derive information about planing stability and stability criteria otherwise difficult to observe. In most cases, 3 to 4 design variables were investigated at a time in the literature. In this study, 7 and 12 variables were investigated.
- Applied Self-Organizing Map Based Adaptive Sampling (SOMBAS) to efficiently investigate design variable sets for which stable planing behavior is obtained for a given speed. This showed that obtaining a group of stable solutions can be used to find new design rules or trade-offs between design parameters.
 - A band of unstable locations for the center of gravity in longitudinal direction l_{cg} .
 - Relation between longitudinal and vertical locations of the center of gravity, l_{cg} and vcg to satisfy certain stability condition.
 - Relation between Beam B and vcg to satisfy certain stability condition.
- Obtained new insights into planing stability.

Chapter 4 Conclusion

- Analysis of oscillation modes through root-locus plots, $\Re(\sigma)_{max}$ plots, and Argand plots
- Sensitivity Analysis of the design variables to the stability limit speed U_{lim}
- Obtained agreements between the numerical models' results and the experiments in 2005.
 - Fairly good quantitative agreement of stability limit speed despite its sensitivity and dimensional uncertainty in rigid-support case.
 - Agreement of the direction towards which the center of gravity must be moved in order to stabilize porpoising.
 - Phase of the oscillation qualitatively agrees in porpoising oscillations of the rigid-support case.
 - Qualitative agreement in the fact that flexible supports mitigate porpoising.

4.3. Potential Developments

Active and semi-active control of the flexible support [38, 34] can be considered to obtain the desired dynamics in both waveless and wavy conditions. For example, Skyhook methods in which damping is controlled to emulate the dynamics of bodies whose damper is attached to an imaginary inertial frame (hence Skyhook) could be employed. This may be effective in eliminating porpoising as well as improving operational reliability in wavy conditions. Of course, it comes at the cost of added weight and complexities.

It would be also important to conduct high-fidelity simulations using Computational Fluid Dynamics (CFD) and Finite Element Methods (FEM). The thesis investigated can be formulated as a challenging but interesting problem of fluid-structure interaction problem as well as two-phase flow (air and water). The computational costs of such investigation may hinder broad parametric investigation but

may provide an important supporting information to the physical experiments, giving insights not readily obtained from the physical experiments alone. Furthermore, their quantitative results provide an additional reference for assessing and improving model accuracies and building regression functions.

Once validated, the parametric models (flexible or rigid) equip us with the means to conduct various trade-off studies concerning porpoising at early design stages. These should provide more informed design decisions than the rules of thumbs hitherto available. With the inclusion of aerodynamic forces, they will be useful in assessing the sizing, location and incidence angles of the lifting surfaces with respect to planing hulls, and whether the flexible support would be needed. Eventually, a new set of design standards could be drawn concerning the longitudinal stability of waterborne seaplanes including the design of flexible support systems.

4.4. Closing Remarks

The numerical analysis of the Linear-Time-Invariant model revealed useful information to the questions posed. The computation shows that whether one should move the center of gravity backward or forward will depend on the position of the center of gravity with respect to the step of the planing hull. If a flexible support is employed one may postpone the inception of porpoising to a much higher Froude number. The simulation results indicate that damping coefficients, as well as spring coefficients in the flexible supports, play an important role and the range of planing speed will determine their values. The damping in the hind support was more effective than the damping in the front support. These numerical results can be used to conduct more dedicated physical experiments to quantitatively assess the numerical models and confirm physical phenomena. Furthermore, aerodynamic effects must be taken into account. These will constitute the future work of this study along with the parametric optimization of the system.

It is hoped that this thesis provides a way to make the hazard of porpoising less critical and avoidable by design instead of by pilot training, thereby helping in making seaplanes more safe and viable. This is in line with the goal of making

seaplanes a point-to-point transportation system to alleviate transport congestion. Not to mention in aiding the operations of seaplanes in emergency and specialized missions.

Appendix A

Overview of Hydrodynamic Calculations

The computation of stability takes two steps. First, the equilibrium or the trim position needs to be found given the planing speed. Second, the small perturbation analysis is performed about the equilibrium position by looking at the increment in force and moment with respect change in state vector variables. As in Flight Dynamics, the stability derivatives need to be obtained about this equilibrium point. We will follow closely the procedure given in Faltinsen [4]. A big part of the following is due to Savitsky [24] and Wagner [27].

A.1. Trim Determination

For trim determination, the following equilibria hold. Vertical forces,

$$Mg = N \cos \tau + T \sin(\tau + \epsilon) - R_v \sin \tau. \quad (\text{A.1})$$

Horizontal forces,

$$T \cos(\tau + \epsilon) = R_v \cos \tau + N \sin \tau. \quad (\text{A.2})$$

Pitching moments,

$$Nc + R_v a - Tf = 0. \quad (\text{A.3})$$

The N represents the resultant hydrodynamic pressure force (represented to be acting at a point along and perpendicular to the keel line in the vertical xz plane). The T is the thrust force from the power plant. These two forces can be expressed with respect to τ , and R_v using the equations (A.1) and (A.2) (ϵ is given by the design). The R_v is the frictional force exerted on the planing surface. Then these

Chapter A Overview of Hydrodynamic Calculations

can be plugged into the moment force equation (A.3) to obtain an equation of a , c , τ , and R_v (f is given by the design),

$$\frac{c}{\cos \tau} \left(Mg - \frac{Mg \sin \tau + R_v}{\cos \epsilon} \sin(\tau + \epsilon) + R_v \sin \tau \right) + R_v a - \frac{Mg \sin \tau + R_v}{\cos \epsilon} f = 0. \quad (\text{A.4})$$

The frictional force is given by

$$R_v = \frac{1}{2} \rho C_F S (U \cos \tau)^2 \simeq \frac{1}{2} \rho C_F S U^2 \quad (\text{A.5})$$

where ρ is water density, S is the wetted surface area and C_F is the friction coefficient.

$$C_F = \frac{0.075}{(\log_{10}(R_n) - 2)^2} + \frac{44 \left[\left(\frac{AHR}{L_K} \right)^{1/3} - 10R_n^{-1/3} \right] + 0.125}{10^3}. \quad (\text{A.6})$$

where AHR is the average hull roughness in micrometers. We set to $AHR = 150$ [μm]. The R_n is the Reynolds number based on the characteristic length L_K which is the wetted keel length. The wetted area S is given as following.

$$S = \frac{\tan^2 \beta}{\sin \beta} \frac{B^2}{4 \left(1 + \frac{z_{\max}}{V_t} \right) \tau} + \frac{B}{\cos \beta} L_C, \quad (\text{A.7})$$

where $1 + \frac{z_{\max}}{V_t} \simeq \pi/2$ for small β (for large β , see [4, p. 303]), and L_C is the wetted chine length. Note that R_v is a function of τ , L_K and L_C which we don't know. The two moment arm lengths a and c pertaining to the hull frictional force R_v and hydrodynamic pressure force N respectively can be formulated as following,

$$a = v_{cg} - \frac{B}{4} \tan(\beta), \quad (\text{A.8})$$

$$c = l_{cg} - l_p. \quad (\text{A.9})$$

The a is fixed given CG location, B , and β , but to get c , we need to determine the distance of center of hydrodynamic pressure from the step l_p . To determine l_p , we take three steps. First, we determine C_{L_0} using

$$C_{L_\beta} = \frac{F_{L_\beta}}{0.5 \rho U^2 B^2} = C_{L_0} - 0.0065 \beta_{deg} C_{L_0}^{0.60} \quad (\text{A.10})$$

where $F_{L_\beta} = Mg$. Second, given F_{n_B} we can obtain λ_W from

$$C_{L_0} = \frac{F_{L_0}}{0.5 \rho U^2 B^2} = \tau_{deg}^{1.1} \left[0.012 \lambda_W^{0.5} + 0.0055 \frac{\lambda_W^{2.5}}{F_{n_B}^2} \right]. \quad (\text{A.11})$$

Again, we do not know the value for τ_{deg} . Thus, we temporarily assume some value for τ_{deg} . Third, the following equation gives l_p .

$$\frac{l_p}{\lambda_W B} = 0.75 - \frac{1}{\frac{5.21 F_{nB}^2}{\lambda_W^2} + 2.39}. \quad (\text{A.12})$$

With the λ_W computed using assumed $\tau = \pi \tau_{deg}/180$, we can also obtain L_K and L_C from

$$\lambda_W = \frac{L_K + L_C}{2B}, \quad (\text{A.13})$$

$$\frac{B}{2} = \frac{\pi}{2 \tan \beta} (L_K - L_C) \tau. \quad (\text{A.14})$$

These enable us to compute R_v for the assumed τ . We now check if equation (A.4) holds. We iterate the process using Brent's method until we find a good τ .

A.2. Stability Derivatives

Based on the trim condition obtained for a given planing speed U , we can now proceed to the calculation of the stability derivatives. The restoring force coefficients due to heave C_{33} and pitch C_{35} are given by

$$\frac{C_{33}}{0.5 \rho U^2 B} = -B \frac{\partial C_{L\beta}}{\partial \eta_3} \Big|_0 = -B \frac{\partial C_{L_0}}{\partial \eta_3} \Big|_0 \left[1 - 0.0039 \beta_{deg} C_{L_0}^{-0.4} \right], \quad (\text{A.15})$$

$$\frac{C_{35}}{0.5 \rho U^2 B} = -B \frac{\partial C_{L\beta}}{\partial \eta_5} \Big|_0 = -B \frac{\partial C_{L_0}}{\partial \eta_5} \Big|_0 \left[1 - 0.0039 \beta_{deg} C_{L_0}^{-0.4} \right], \quad (\text{A.16})$$

where $|_0$ denotes “at the static equilibrium position” and

$$\frac{\partial C_{L_0}}{\partial \eta_3} \Big|_0 = \tau_{deg}^{1.1} \left[0.006 \lambda_0^{-0.5} + \frac{0.01375 \lambda_0^{1.5}}{F_{nB}^2} \right] \frac{\partial \lambda_W}{\partial \eta_3} \Big|_0, \quad (\text{A.17})$$

$$\begin{aligned} \frac{\partial C_{L_0}}{\partial \eta_5} \Big|_0 &= 1.1 \left(\frac{180}{\pi} \right)^{1.1} \tau^{0.1} \left[0.012 \lambda_0^{0.5} + \frac{0.0055 \lambda_0^{2.5}}{F_{nB}^2} \right] \\ &\quad + \tau_{deg}^{1.1} \left[0.006 \lambda_0^{-0.5} + \frac{0.01375 \lambda_0^{1.5}}{F_{nB}^2} \right] \frac{\partial \lambda_W}{\partial \eta_5} \Big|_0. \end{aligned} \quad (\text{A.18})$$

Here, λ_0 is the value of λ_W at the static equilibrium. Furthermore,

$$\frac{\partial \lambda_W}{\partial \eta_3} \Big|_0 = -\frac{1}{\sin \tau} \frac{1}{B}, \quad (\text{A.19})$$

$$\frac{\partial \lambda_W}{\partial \eta_5} \Big|_0 = \frac{-vcg/B}{\sin^2 \tau} + \frac{z_{wt}/B}{\sin^2 \tau} \cos \tau + \frac{0.25 \tan \beta}{(1 + z_{\max}/Vt) \tau^2}. \quad (\text{A.20})$$

Chapter A Overview of Hydrodynamic Calculations

From equation (A.12), we can write

$$\left. \frac{1}{B} \frac{\partial l_p}{\partial \lambda_w} \right|_0 = 0.75 - \frac{15.63 \frac{F_{nB}^2}{\lambda_0^2} + 2.39}{\left(5.21 \frac{F_{nB}^2}{\lambda_0^2} + 2.39 \right)^2}. \quad (\text{A.21})$$

Then, we can compute the pitch moment coefficients due to heaving C_{53} and due to pitching C_{55} as

$$\frac{C_{53}}{0.5\rho U^2 B^2} = - \left[\frac{1}{B} \frac{\partial l_p}{\partial \lambda_w} B \frac{\partial \lambda}{\partial \eta_3} C_{L\beta} + \left(\frac{l_p}{B} - \frac{l_{cg}}{B} \right) B \frac{\partial C_{L\beta}}{\partial \eta_3} \right]_0, \quad (\text{A.22})$$

$$\frac{C_{55}}{0.5U^2 B^3} = - \left[\frac{1}{B} \frac{\partial l_p}{\partial \lambda_w} \frac{\partial \lambda_w}{\partial \eta_5} C_{L\beta} + \left(\frac{l_p}{B} - \frac{l_{cg}}{B} \right) \frac{\partial C_{L\beta}}{\partial \eta_5} \right]_0. \quad (\text{A.23})$$

The added mass calculations are divided into two hull regions: the region where the keel is wet but the chine is not (the triangular planform region) and the region thereafter up to the step where the planing surface is completely wet (the rectangular planform region). Strip theory is used to exploit two-dimensional analytical solutions. A two-dimensional added mass of a wedge can be given using Gamma function,

$$a_{33} \equiv \rho d^2 K = \frac{\rho d^2}{\tan \beta} \left[\frac{\pi}{\sin \beta} \frac{\Gamma(1.5 - \frac{\beta}{\pi})}{\Gamma^2(1 - \frac{\beta}{\pi}) \Gamma(0.5 + \frac{\beta}{\pi})} - 1 \right] \quad (\text{A.24})$$

where d is the draft and we only consider the real part of K . The d is defined as the draft from the spray root position,

$$d = \left(1 + \frac{z_{max}}{V_t} \right) x \tau. \quad (\text{A.25})$$

Here, x is on the axis that increases towards the step along the keel line with origin at the point where the wetting of keel starts. In particular, we denote x_s as the point at which chine wetting starts. The added mass in the heaving of the triangular region is obtained from

$$A_{33}^{(1)} = \rho K \left(1 + \frac{Z_{max}}{V_t} \right) \tau^2 \int_0^{x_s} x^2 dx \quad (\text{A.26})$$

where

$$x_s = \frac{B}{2} \frac{\tan \beta}{\left(1 + \frac{Z_{max}}{V_t} \right) \tau} \quad (\text{A.27})$$

After integration, we have

$$\frac{A_{33}^{(1)}}{\rho B^3} = \frac{K}{24} \frac{\tan^3 \beta}{\left(1 + \frac{Z_{max}}{V_t} \right) \tau}. \quad (\text{A.28})$$

A.2 Stability Derivatives

For the pitch induced added mass in the triangular region,

$$A_{35}^{(1)} = A_{53}^{(1)} = -\rho K \int_0^{x_s} d^2(x - x_G) dx \quad (\text{A.29})$$

where $x_G = L_K - l_{cg}$. After integration, we obtain

$$\frac{A_{35}^{(1)}}{\rho B^4} = \frac{A_{53}^{(1)}}{\rho B^4} = \frac{A_{33}^{(1)}}{\rho B^3} \frac{x_G}{B} - \frac{K}{64} \frac{\tan^4 \beta}{\left(1 + \frac{z_{max}}{V_t}\right)^2 \tau^2}. \quad (\text{A.30})$$

We also have

$$A_{55}^{(1)} = \rho K \int_0^{x_s} d^2(x - x_G)^2 dx, \quad (\text{A.31})$$

which results in

$$\frac{A_{55}^{(1)}}{\rho B^5} = \frac{K}{160} \frac{\tan^5 \beta}{\left(1 + \frac{z_{max}}{V_t}\right)^3 \tau^3} - \frac{K}{32} \frac{x_G}{B} \frac{\tan^4 \beta}{\left(1 + \frac{z_{max}}{V_t}\right)^2 \tau^2} + \left(\frac{x_G}{B}\right)^2 \frac{A_{33}^{(1)}}{\rho B^3}. \quad (\text{A.32})$$

As for the rectangular region, the heaving induced part is given by

$$\frac{A_{33}^{(2)}}{\rho B^3} = C_1 \frac{\pi}{8} \frac{L_C}{B} \quad (\text{A.33})$$

where

$$C_1 = \frac{2 \tan^2 \beta}{\pi} K. \quad (\text{A.34})$$

The pitching induced added masses of the rectangular portion are

$$\frac{A_{35}^{(2)}}{\rho B^4} = \frac{A_{53}^{(2)}}{\rho B^4} = -C_1 \frac{\pi}{16} \left[\left(\frac{L_K}{B}\right)^2 - \left(\frac{x_s}{B}\right)^2 \right] + \frac{x_G}{B} \frac{A_{33}^{(2)}}{\rho B^3} \quad (\text{A.35})$$

and

$$\frac{A_{55}^{(2)}}{\rho B^5} = \frac{C_1 \pi}{24} \left[\left(\frac{L_K}{B}\right)^3 - \left(\frac{x_s}{B}\right)^3 \right] - \frac{C_1 \pi}{8} \left(\frac{x_G}{B}\right) \left[\left(\frac{L_K}{B}\right)^2 - \left(\frac{x_s}{B}\right)^2 \right] + \left(\frac{x_G}{B}\right)^2 \frac{A_{33}^{(2)}}{\rho B^3}. \quad (\text{A.36})$$

The resulting added masses are given by $A_{ij} = A_{ij}^{(1)} + A_{ij}^{(2)}$.

The damping coefficients B_{ij} are analysed using a quasi-steady approach in which changes in the angle of attack immediately cause changes in lift. We exclude hydrostatic effects in equations (A.10) and (A.11) by setting $F_{nB} \rightarrow \infty$.

$$C_{L\beta} = C_{L_0} - 0.0065 \beta_{deg} C_{L_0}^{0.60}, \quad (\text{A.37})$$

where

$$C_{L_0} = \left(\frac{180}{\pi}\right)^{1.1} \tau^{1.1} 0.012 \lambda_W^{0.5}. \quad (\text{A.38})$$

Chapter A Overview of Hydrodynamic Calculations

Because of the heave velocity, there is a change in angle of attack (trim)

$$\alpha = -\frac{d\eta_3}{dt}/U = -\frac{\dot{\eta}_3}{U}. \quad (\text{A.39})$$

This causes a vertical force

$$F_3 = -\frac{1}{2}\rho U^2 B^2 \frac{\partial C_{L_\beta}}{\partial \tau} \frac{\dot{\eta}_3}{U} \quad (\text{A.40})$$

where

$$\frac{\partial C_{L_\beta}}{\partial \tau} = \frac{\partial C_{L_0}}{\partial \tau} \left[1 - 0.0039\beta_{deg} C_{L_0}^{-0.4} \right] \quad (\text{A.41})$$

and

$$\frac{\partial C_{L_0}}{\partial \tau} = 0.0132 \left(\frac{180}{\pi} \right)^{1.1} \tau^{0.1} \lambda_W^{0.5}. \quad (\text{A.42})$$

Note the $\dot{\eta}_3$ in equation (A.40). This gives the heaving damping force,

$$\frac{B_{33}}{\rho B^3 \left(\frac{g}{B} \right)^{\frac{1}{2}}} = 0.5 F_{nB} \frac{\partial C_{L_\beta}}{\partial \tau}. \quad (\text{A.43})$$

The pitching moment resulting from the heave velocity can be computed using

$$F_5 = F_3 (0.75 \lambda_W B - l_{cg}) \quad (\text{A.44})$$

and this gives

$$\frac{B_{53}}{B_{33} B} = 0.75 \lambda_W - \frac{l_{cg}}{B}. \quad (\text{A.45})$$

The damping coefficients B_{55} and B_{35} are studied with respect to $d\eta_5/dt$ [39], and given as

$$B_{55} = U x_T^2 a_{33}(x_T), \quad (\text{A.46})$$

$$B_{35} = U A_{33} - U x_T a_{33}(x_T). \quad (\text{A.47})$$

where

$$a_{33}(x_T) = \rho \left(\frac{B \tan \beta}{2} \right)^2 K \quad (\text{A.48})$$

is the two dimensional added mass in heave for the cross section at step $x_T = l_{cg}$.

Appendix B

Dimensional Analysis

To infer full-size phenomena from tow-tank experiments and to reduce the number of experiments, it is useful to non-dimensionalize relevant variables. In this section, we perform a dimensional analysis based on the Buckingham's π theorem [40]. White [41] gives a detailed introduction on how to do it.

Let the eigenvalue of the planing craft be determined by some function f with the following arguments.

$$\sigma = f(U, M, I_{55}, \beta, \tau, B, vcg, L_K, L_C, l_{cg}, l_p, C_{L_0}, C_{L_\beta}, \lambda_W, \rho, g) \quad (\text{B.1})$$

We choose B , g , M as scaling parameters. Their dimensions are shown in Table B.1.

Using the three scaling parameters, we can make the other variables dimensionless. The other variables that have dimensions are listed in Table B.2.

B.1. Non-Dimensional Parameter Group

We start by non-dimensionalizing σ . Using the scaling parameters, one can express the first non-dimensional parameter π_1 as following.

$$\pi_1 = B^a g^b M^c \sigma, \quad (\text{B.2})$$

B	g	M
L	LT^{-2}	M

Table B.1: Scaling parameters and their dimensions: L is length, T is time (not thrust), and M is mass.

Chapter B Dimensional Analysis

σ	U	I_{55}	vcg	L_K	L_C	l_{cg}	l_p	λ_w	ρ
T^{-1}	LT^{-1}	ML^2	L	L	L	L	L	L	ML^{-3}

Table B.2: Other variables and their dimensions.

where a, b, c are integer exponent we want to identify to make the expression of π_1 dimensionless. Then, the following must hold,

$$L^a(LT^{-2})^b M^c T^{-1} = L^{a+b} M^c T^{-2b-1} = L^0 M^0 T^0. \quad (B.3)$$

Thus,

$$\begin{aligned} a + b &= 0, \\ c &= 0, \\ -2b - 1 &= 0. \end{aligned}$$

This gives $a = -b = \frac{1}{2}$, $c = 0$, and the resulting expression is

$$\pi_1 = B^{\frac{1}{2}} g^{-\frac{1}{2}} M^0 \sigma = \sqrt{\frac{B}{g}} \sigma. \quad (B.4)$$

For $\pi_2 = B^a g^b M^c U$, we need $L^a(LT^{-2})^b M^c(LT^{-1}) = L^{a+b+1} M^c T^{-2b-1} = L^0 M^0 T^0$.

This results in $a = b = -\frac{1}{2}$, $c = 0$, and we have

$$\pi_2 = B^{-\frac{1}{2}} g^{-\frac{1}{2}} M^0 U = \frac{U}{\sqrt{gB}}. \quad (B.5)$$

For $\pi_3 = B^a g^b M^c I_{55}$, we need $L^a(LT^{-2})^b M^c(ML^2) = L^{a+b+2} M^{c+1} T^{-2b} = L^0 M^0 T^0$.

This results in $a = -2$, $b = 0$, $c = -1$, and we have

$$\pi_3 = B^{-2} g^0 M^{-1} I_{55} = \frac{I_{55}}{MB^2}. \quad (B.6)$$

From vcg to λ_w in Table B.2, they can be scaled using B because they are all lengths. Thus, $\pi_4 = \frac{vcg}{B}$, $\pi_5 = \frac{L_K}{B}$, $\pi_6 = \frac{L_C}{B}$, $\pi_7 = \frac{l_{cg}}{B}$, $\pi_8 = \frac{l_p}{B}$, and $\pi_9 = \frac{\lambda_w}{B}$.

For $\pi_{10} = B^a g^b M^c \rho$, we need $L^a(LT^{-2})^b M^c(ML^{-3}) = L^{a+b-3} M^{c+1} T^{-2b} = L^0 M^0 T^0$.

This results in $a = 3$, $b = 0$, $c = -1$, and we have

$$\pi_{10} = B^3 g^0 M^{-1} \rho = \frac{B^3}{M} \rho. \quad (B.7)$$

B.1 Non-Dimensional Parameter Gropus

In flexible-support case, we have spring stiffness coefficients k_f, k_b and damping coefficients c_f, c_b . Stiffness coefficients have units of N/m . Dimensionally, it is MT^{-2} . The damping coefficients' unit is Ns/m and its dimension is MT^{-1} . So the dimensionless versions can be expressed as

$$\pi_{11,12} = \frac{B}{gM} k_{f,b} \quad (B.8)$$

$$\pi_{13,14} = \sqrt{\frac{B}{g}} \frac{c_{f,b}}{M} \quad (B.9)$$

Appendix C

Root-Locus Plots and $\Re(\sigma)_{max}$ Plots of Various Support Configurations

Following plots are root-locus and $\Re(\sigma)_{max}$ Plots with F_{nB} varied up to 10.138 as a variable. In the root-locus plot, The cross dots are for the rigid-support-case and the round dots are for the flexible-support case.

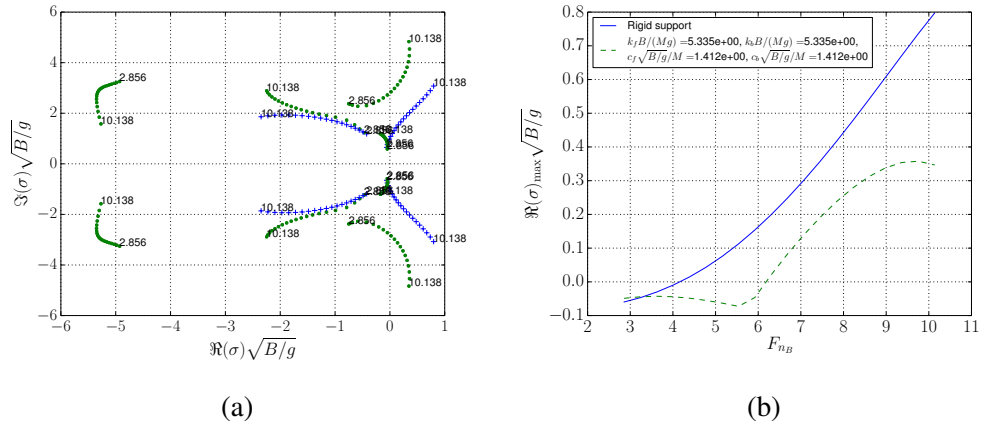


Figure C.1: $k_{f,b} = 2117 [N/m]$, $c_{f,b} = 80 [N s/m]$

Chapter C Root-Locus Plots and $\Re(\sigma)_{max}$ Plots of Various Support Configurations

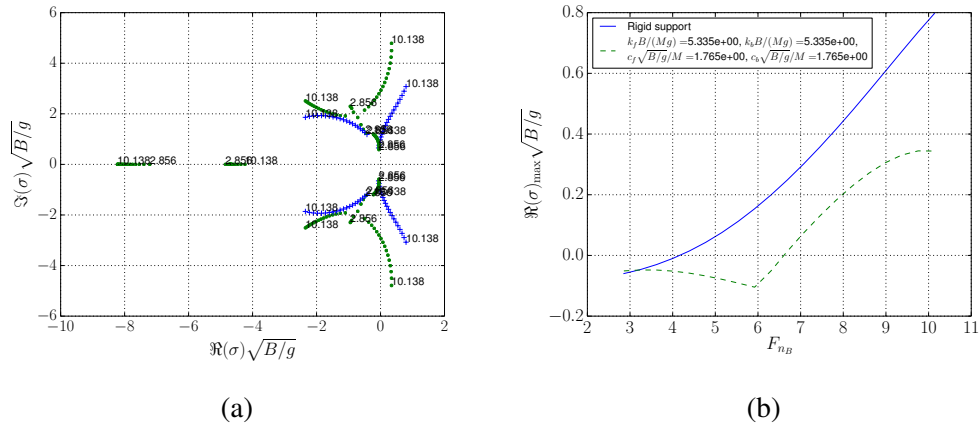


Figure C.2: $k_{f,b} = 2117$ [N/m], $c_{f,b} = 100$ [N s/m]

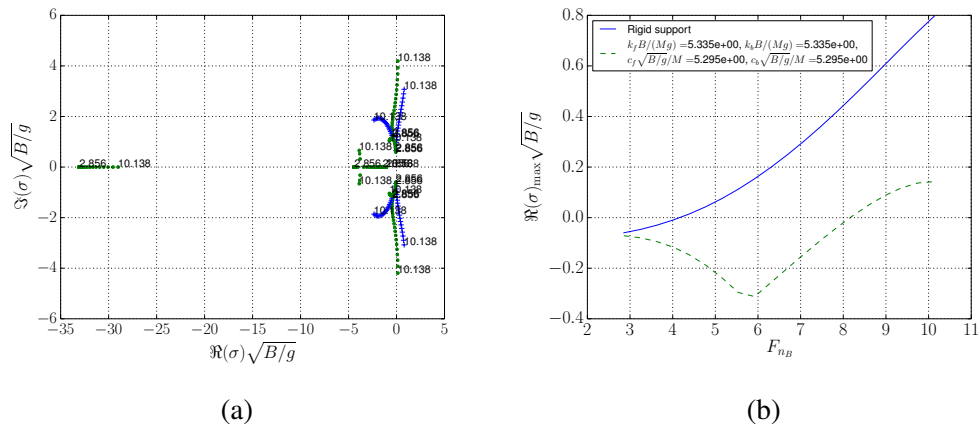


Figure C.3: $k_{f,b} = 2117$ [N/m], $c_{f,b} = 300$ [N s/m]

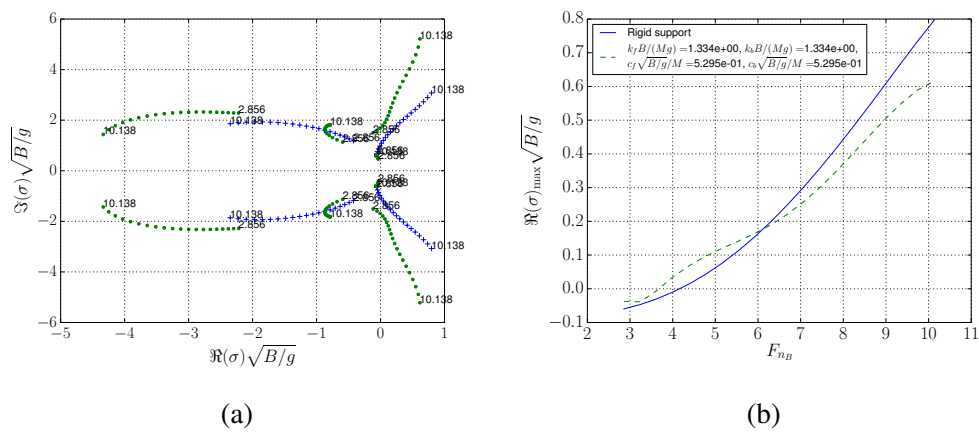
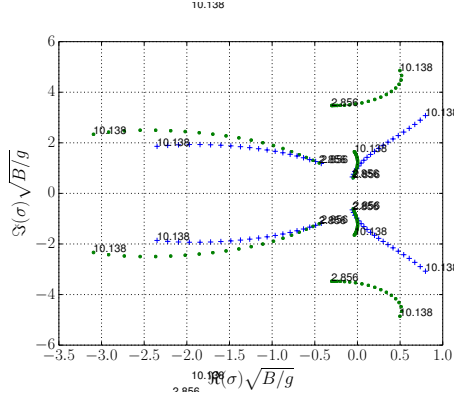
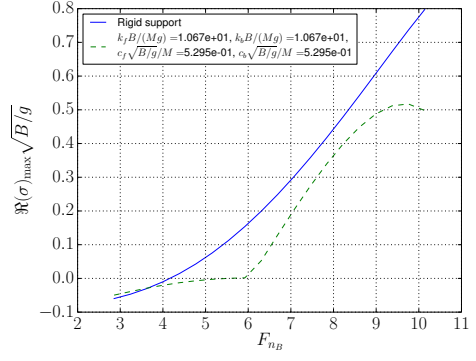


Figure C.4: $k_{f,b} = 529 \text{ [N/m]}$, $c_{f,b} = 30 \text{ [N s/m]}$

C.0 Non-Dimensional Parameter Groups

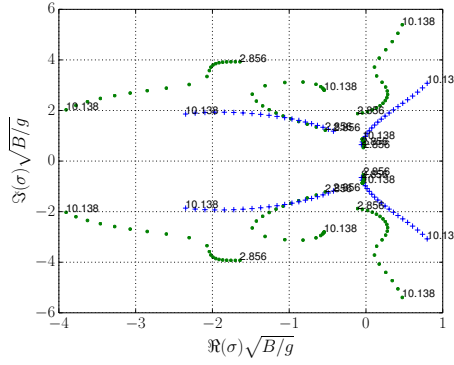


(a)

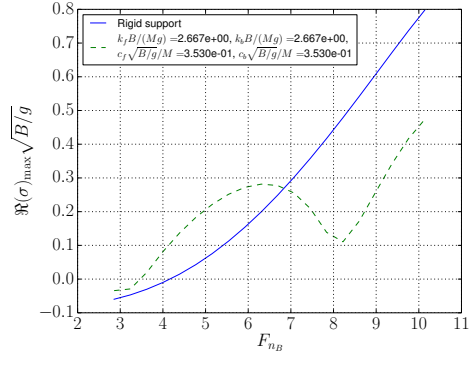


(b)

Figure C.5: $k_{f,b} = 4234$ [N/m], $c_{f,b} = 30$ [N s/m]

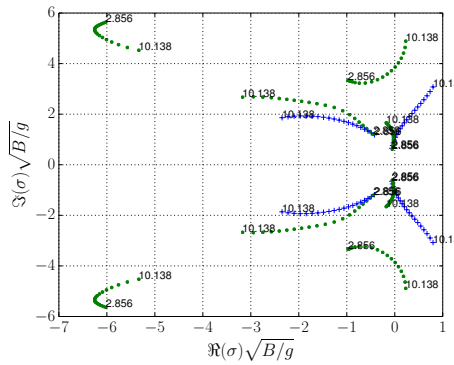


(a)

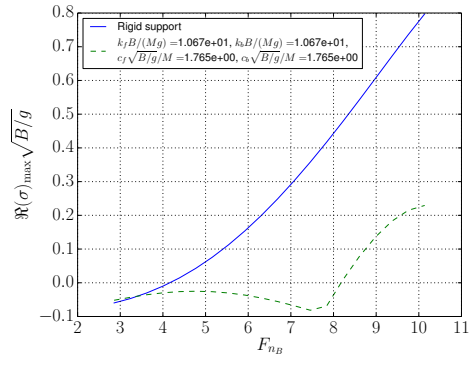


(b)

Figure C.6: $k_{f,b} = 1058$ [N/m], $c_{f,b} = 20$ [N s/m]



(a)



(b)

Figure C.7: $k_{f,b} = 4234$ [N/m], $c_{f,b} = 100$ [N s/m]

Chapter C Root-Locus Plots and $\Re(\sigma)_{\max}$ Plots of Various Support Configurations

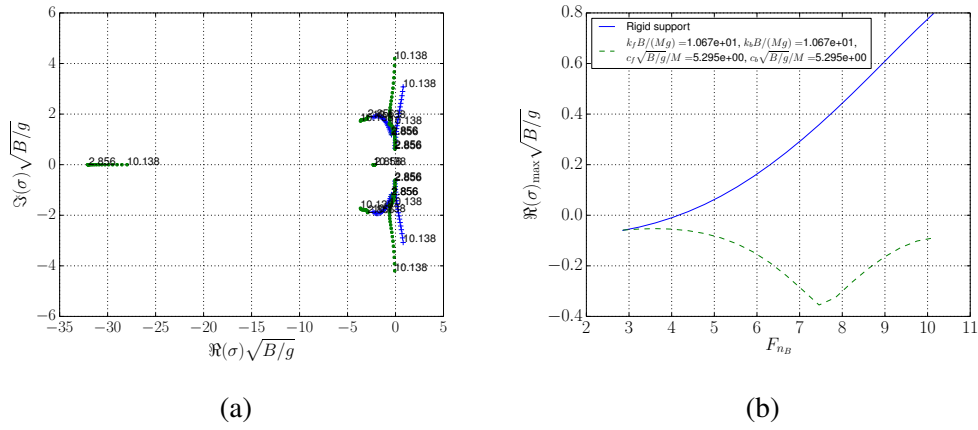


Figure C.8: $k_{f,b} = 4234 \text{ [N/m]}$, $c_{f,b} = 300 \text{ [N s/m]}$

Appendix D

SOMBAS

Algorithm 1 SOM BASED ADAPTIVE SAMPLING

- 1: Generate N samples to create initial training set
 - 2: **while** Termination condition not met **do**
 - 3: Train SOM using the normalized training set
 - 4: **for all** cells satisfying SELECTION CONDITION **do**
 - 5: Perturb the weight vectors of the selected cells according to MUTATION
 - 6: **end for**
 - 7: Un-normalize the perturbed samples
 - 8: Evaluate true output of the perturbed and unperturbed samples
 - 9: UPDATE TRAINING SET
 - 10: **end while**
-

Algorithm 2 SELECTION CONDITION

- 1: Let y_{\min} be the smallest output in the training set X , \hat{y} be output from a cell weight vector, and T_s be the selectivity parameter (or Temperature)
 - 2: Generate a uniform random number $0 \leq r < 1$ and check the following:
 - 3: **if** $r < \exp\left(\frac{y_{\min} - \hat{y}}{T_s}\right)$ **then**
 - 4: Corresponding weight vector is selected
 - 5: **end if**
-

Algorithm 3 MERIT FUNCTION

- 1: Let L denote the value below which objective or output y is considered to be “good enough”, \mathbf{s} denote a weight vector (\mathbf{x}^T, \hat{y}) from SOM, and $\mathbf{t}(m)$, $m = 1, 2, \dots, M_t$ denote the training samples
 - 2: **if** Trunc is specified **then**
 - 3: Normalize L (\mathbf{s} , and \mathbf{t}_i are already normalized)
 - 4: $\hat{y} \leftarrow \max(L, \hat{y}) - \rho \min(\|\mathbf{s} - \mathbf{t}(m)\|_2)$
 - 5: Normalize \hat{y}
 - 6: **end if**
 - 7: Use this \hat{y} in SELECTION CONDITION
-

Algorithm 4 MUTATION

- 1: Let F_c be contraction factor and F_e be expansion factor
 - 2: Let P_m be mutation probability
 - 3: Given training samples, compute covariance matrix C , and let the covariance matrix from previous iteration be C_{old}
 - 4: **if** current $y_{\min} < \text{previous } y_{\min}$ **then**
 - 5: $C = F_e (0.2C + 0.8C_{\text{old}})$
 - 6: **else**
 - 7: $C = F_c (0.2C + 0.8C_{\text{old}})$
 - 8: **end if**
 - 9: For each selected sample, perturb it by sampling from multivariate normal distribution with center at the selected sample with covariance C .
 - 10: Replace a parameter in the selected vectors with the mutated one at probability of P_m
-

Algorithm 5 UPDATE TRAINING SET 1

- 1: Add the perturbed samples to the training set
 - 2: **if** Training set sample size larger than maximum sample size **then**
 - 3: Sort the training set with respect to output value
 - 4: Remove the worst samples to make the training sample size equal to maximum sample size
 - 5: **end if**
-

Algorithm 6 UPDATE TRAINING SET 2

- 1: **for all** perturbed weight vectors' response y_p **do**
 - 2: Randomly pick one of the training sample, and obtain its response y_t
 - 3: Obtain d_p , the nearest neighbor distance of perturbed sample to sampled points thus far and d_t the nearest neighbor distance of the training sample to sampled points thus far
 - 4: **if** $\max(L, y_p) = \max(L, y_t)$ and $d_p > d_t$ **then**
 - 5: Replace the training sample with the perturbed weight vector
 - 6: **else if** $y_p < y_t$ **then**
 - 7: Replace the training sample with the perturbed weight vector
 - 8: **end if**
 - 9: **end for**
-

Bibliography

- [1] Keiichi Ito, Yoshiaki Hirakawa, Tsugukiyo Hirayama, Tatsumi Sakurai, and Tom Dhaene. Longitudinal stability augmentation of seaplanes in planing. In *Proceedings of AIAA Modeling and Simulation Technologies Conference (Aviation 2015)*, Dallas, Texas, June 22 - 26 2015. AIAA.
- [2] Keiichi Ito, Yoshiaki Hirakawa, Tsugukiyo Hirayama, Tatsumi Sakurai, and Tom Dhaene. Longitudinal stability augmentation of seaplanes in planing. *AIAA Journal of Aircraft*, 53(5):1332–1342, 2016.
- [3] Yoshiaki Hirakawa, Takehiko Takayama, Asuka Kosaki, Hiromitsu Kikuchi, Tsugukiyo Hirayama, and Tatsumi Sakurai. Model experiment of a suppression-system for wave impact and porpoising phenomena. *Conference Proceedings of The Japan Society of Naval Architects and Ocean Engineers (in Japanese)*, 3:239–242, 2006.
- [4] Odd M. Faltinsen. *Hydrodynamics of High-Speed Marine Vehicles*. Cambridge University Press, 2005.
- [5] Keiichi Ito, Tom Dhaene, Naji El Masri, Roberto d’Ippolito, and Joost Van de Peer. Self-organizing map based adaptive sampling. In *Proceedings of 5th International Conference on Experiments/Process/System Modeling/Simulation/Optimization (5th IC-EpsMsO)*, volume II, pages 504 – 513, Athens, Greece, July 3 - 6 2013. ISBN:978-618-80527-2-7 or 978-618-80527-0-3.

- [6] Keiichi Ito, Ivo Couckuyt, Roberto d’Ippolito, and Tom Dhaene. Design space exploration using self-organizing map based adaptive sampling. *Applied Soft Computing*, 43:337 – 346, June 2016.
- [7] Keiichi Ito. *Sampling High-Dimensional Design Spaces for Analysis and Optimization*. PhD thesis, Ghent University, December 2016. ISBN: 978-90-8578-952-9.
- [8] John B. Parkinson. Appreciation and determination of the hydrodynamic qualities of seaplanes. Technical Note 1290, National Advisory Committee for Aeronautics, Washington, May 1947.
- [9] Charles L. Shuford, Jr. A theoretical and experimental study of planing surfaces including effects of cross section and plan form. Report 1355, National Advisory Committee for Aeronautics, 1958.
- [10] H. M. Garner. Porpoising test on a model of a flying boat hull. Reports and Memoranda 1492, Marine Aircraft Experimental Establishment, March 1932.
- [11] K. M. Tomaszewski. Hydrodynamic design of seaplane floats. Current papers, Ministry of Supply Aeronautical Research Council, 1950.
- [12] Dale De Remer. *Water Flying Concepts: an Advanced Text on Wilderness Water Flying*. Aviation Supplies & Academics, Newcastle, Washington, 2nd edition, 1990.
- [13] Burke Mees. *Notes of a Seaplane Instructor*. Aviation Supplies & Academics, Newcatle, Washington, 1998.
- [14] Alexander Klemlin, John D. Pierson, and Edmund M. Storer. An introduction to seaplane porpoising. *Journal of the Aeronautical Sciences*, 6(8):1905–1915, June 1939.
- [15] A. G. Smith and H. G. White. A review of porpoising instability of seaplanes. A.R.C. Technical Report 2852, Aeronautical Research Council, London: Her Majesty’s Stationery Office, February 1944.

- [16] W. G. A. Perring and H. Glauert. The stability on the water of a seaplane in the planing condition. Reports and Memoranda 1493, Royal Aircraft Establishment, June 1932.
- [17] John B. Parkinson and John R. Dawson. Tank tests of n.a.c.a. model 40 series of hulls for small flying boats and amphibians. Technical Report 543, National Advisory Committee for Aeronautics, Langley Aeronautical Lab, January 1937.
- [18] James M. Benson and Lindsay J. Lina. The effect of dead rise upon the low-angle type porpoising. Advance restricted report, National Advisory Committee for Aeronautics, Langley Memorial Aeronautical Laboratory, October 1943.
- [19] James M. Benson and Anton Freihofner. Methods and charts for computing stability derivatives of a v-bottom planing surface. Advance Restricted Report 3L08, National Advisory Committee for Aeronautics, Langley Memorial Aeronautical Laboratory, 1943.
- [20] James M. Shoemaker. Tank tests of flat and v-bottom planing surfaces. Technical Notes 509, National Advisory Committee for Aeronautics, Langley Memorial Aeronautical Laboratory, November 1934.
- [21] Kenneth S. M. Davidson, F. W. S. Locke, Jr., and Anthony Soares. Porpoising a comparison of theory with experiment. Advance Restricted Report 3G07, National Advisory Committee for Aeronautics, Langley Memorial Aeronautical Laboratory, July 1943.
- [22] Tullio Celano, III. The prediction of porpoising inception for modern planing craft. Trident Report 254, U.S. Naval Academy, Annapolis, MD, U.S.A., 1998.
- [23] Yoshiho Ikeda and Toru Katayama. Porpoising oscillation of very-high-speed marine craft. *Philosophical Transactions of The Royal Society, Series A*, 358(1771):1905–1915, 2000.

- [24] Daniel Savitsky. Hydrodynamic design of planing hulls. *Marine Technology*, 1(1):71 – 96, October 1964.
- [25] Hiroyasu Takemoto. Some considerations on water impact pressure. *Journal of the Society of Naval Architects of Japan*, 1984(156):314–322, 1984.
- [26] Yoshiyuki Yamamoto, Hideomi Ohtsubo, and Yoshihide Kohno. Water impact of wedge model. *Journal of the Society of Naval Architects of Japan*, 1984(155):236–245, 1984.
- [27] Herbert Wagner. Über stoß- und gleitvorgänge an der oberfläche von flüssigkeiten. *Zeitschrift für Angewandte Mathematik und Mechanik*, 12(4):193 – 215, August 1932. In German.
- [28] R Zhao, O Faltinsen, and J Aarsnes. Water entry of arbitrary two-dimensional sections with and without flow separation. In *Proceedings of the 21st symposium on naval hydrodynamics*, pages 408–423. Trondheim, Norway, National Academy Press, Washington, DC, USA, 1996.
- [29] Darrol Stinton. Aero-marine design and flying qualities of floatplanes and flying-boats. *Aeronautical Journal*, pages 97–127, March 1987.
- [30] Serge Abrate. Hull slamming. *Applied Mechanics Reviews*, 64(6):060803–1 – 060803–35, November 2011.
- [31] Virginia Torczon and Michael W. Trosset. Using approximations to accelerate engineering design optimization. Technical report, Institute for Computer Applications in Science and Engineering (ICASE), 1998.
- [32] Nikolaus Hansen and Andreas Ostermeier. Adapting arbitrary normal mutation distributions in evolution strategies: The covariance matrix adaptation. In *Proceedings of the 1996 IEEE Conference on Evolutionary Computation*, pages 312 – 317, 1996.
- [33] Richard P. Brent. *Algorithms for Minimization Without Derivatives*. Prentice-Hall, Englewood Cliffs, NJ, 1973.

- [34] KYB株式会社, editor. 自動車のサスペンション: 構造 理論 評価. グランプリ出版, 2013.
- [35] Toshimitsu Homma and Andrea Saltelli. Importance measures in global sensitivity analysis of nonlinear models. *Reliability Engineering and System Safety*, 52:1 – 17, 1996.
- [36] Andrea Saltelli, Paola Annoni, Ivano Azzini, Francesca Campolongo, Marco Ratto, and Stefano Tarantola. Variance based sensitivity analysis of model output. design and estimator for the total sensitivity index. *Computer Physics Communications*, 181(2):259 – 270, 2010.
- [37] Michiel J.W. Jansen. Analysis of variance designs for model output. *Computer Physics Communications*, 117(1-2):35 – 43, 1999.
- [38] M. Canale, M. Milanese, and C. Novara. Semi-active suspension control using “fast” model-predictive techniques. *Control Systems Technology, IEEE Transactions on*, 14(6):1034–1046, Nov 2006.
- [39] Nils Salvesen, E.O. Tuck, and Odd Faltinsen. Ship motions and sea loads. *SNAME Transactions*, 78:250–287, 1970.
- [40] Edgar Buckingham. On physically similar systems; illustrations of the use of dimensional equations. *Physical Review*, 4(4):345 – 376, 1914.
- [41] Frank M. White. *Fluid Mechanics*. McGraw-Hill, 4th edition, 1999.